


Bidirectional state transfer between superconducting and microwave-photon qubits by single reflection

Kazuki Koshino^{1,*} and Kunihiro Inomata^{2,†}

¹College of Liberal Arts and Sciences, Tokyo Medical and Dental University, Ichikawa, Chiba 272-0827, Japan

²Global Research and Development Center for Business by Quantum-AI Technology (G-QuAT), National Institute of Advanced Industrial Science and Technology (AIST), Tsukuba, Ibaraki 305-8568, Japan

 (Received 9 February 2023; revised 20 February 2024; accepted 12 April 2024; published 23 May 2024)

The number of superconducting qubits contained in a single quantum processor is increasing steadily. However, to realize a truly useful quantum computer, it is inevitable to increase the number of qubits much further by distributing quantum information among distant processors using flying qubits. A key element towards this goal is a deterministic quantum interaction between superconducting-atom and propagating microwave-photon qubits. Here, we confirm the bidirectional state transfer between them, which completes by simply reflecting the photon at the atom. The averaged fidelity of the photon-to-atom (atom-to-photon) state transfer reaches 0.826 (0.801), limited mainly by the lifetime of the atom qubit. The present technology would be useful for future distributed quantum computation with superconducting qubits.

DOI: [10.1103/PhysRevApplied.21.054049](https://doi.org/10.1103/PhysRevApplied.21.054049)

I. INTRODUCTION

The number of solid-state qubits contained in a single processor is steadily increasing [1,2] and has reached three digits recently. However, an incomparably larger number of qubits is required in order to make such quantum machines truly useful. Therefore, in the near future, it would be indispensable to distribute quantum information among remote quantum processors [3–6], using deterministic quantum interactions between stationary and flying qubits [7,8].

In superconducting quantum computation, stationary qubits are encoded on various types of superconducting atoms and flying qubits are encoded on microwave photons propagating in waveguides. The atom-photon interaction in this setup is drastically enhanced due to the natural spatial mode matching between radiation from an atom and a propagating photon in the waveguide [9–15]. Applying this waveguide QED effect, single microwave-photon detection has been accomplished by various schemes [16–21]. Another prominent achievement in this field is the deterministic release and catch of a photon by remote

atoms, which has been applied for remote entanglement generation and a photon-photon gate [22–30]. In these works, the atom-waveguide coupling is actively tuned in accordance with the shape of the photon pulse to achieve a capture probability close to unity.

Recently, we theoretically proposed a deterministic SWAP gate between a superconducting atom and a microwave photon [31]. The working principle of this gate is an essentially passive one, the single-photon Raman interaction [32–39], which is characteristic of waveguide QED setups and guarantees a high-fidelity operation insensitive to the shape and length of the input photon qubit. Besides this point, the present scheme has the following merits for practical implementation.

(1) *Simple setup*—the required system for the present gate is an atom and a resonator coupled in the dispersive regime, each coupled to independent waveguides (Fig. 1). This is a common element in a superconducting quantum processor adopting the dispersive qubit readout [40,41].

(2) *Gate tunability*—although we focus only on the SWAP gate in this work, the present gate functions as a more general (SWAP)^α gate ($0 \leq \alpha \leq 1$) [43–46]. The gate type α is *in situ* tunable through the amplitude and frequency of the drive pulse to the atom [31].

(3) *Dual-rail encoding*—the photon qubit is encoded on its two different carrier frequencies [47–50]. In contrast to single-rail (photon-number) encoding, we can avoid degradation of fidelity by photon loss and sharing a phase reference [51].

*Corresponding author: kazuki.koshino@osamember.org

†Corresponding author: kunihiro.inomata@aist.go.jp

Published by the American Physical Society under the terms of the [Creative Commons Attribution 4.0 International](https://creativecommons.org/licenses/by/4.0/) license. Further distribution of this work must maintain attribution to the author(s) and the published article's title, journal citation, and DOI.

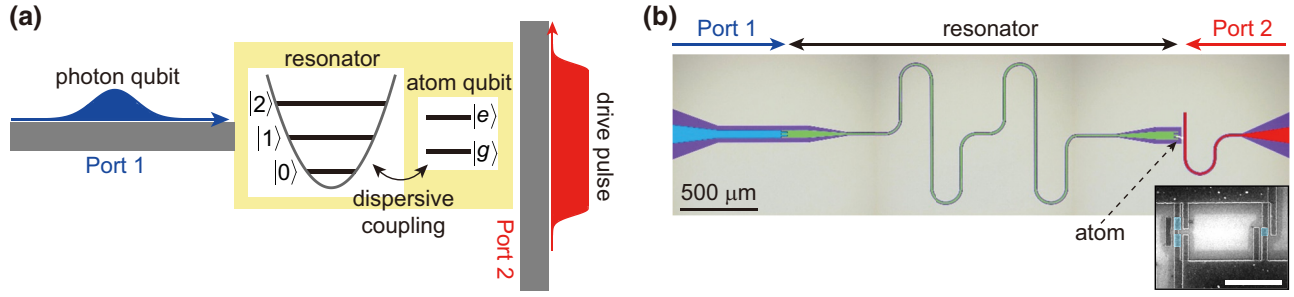


FIG. 1. Setup for the SWAP gate between superconducting-atom and microwave-photon qubits. (a) Schematic of the setup. (b) False-colored optical micrograph of the actual device. Inset shows a scanning electron micrograph of a flux qubit as an atom, in which blue-shaded areas indicate Josephson junctions. Scale bar is $2 \mu\text{m}$.

In this work, as a partial demonstration of the proposed scheme, we confirm the deterministic and bidirectional state transfer between the atom and photon qubits. This completes simply by a single bounce of the photon-qubit pulse at the atom qubit (Fig. 1), and would therefore be useful for distributed quantum computation with superconducting qubits. We note that our results contrast sharply with the state transfer or remote entanglement generation achieved by cascading *unidirectional* quantum state transfer [22–30].

The rest of this paper is organized as follows. In Sec. II, we present the experimental setup to execute the atom-photon SWAP gate and explain its working principle. In Sec. III, we confirm the bidirectional state transfer between the atom and photon qubits. The photon qubit should be in a single-photon state in principle, but we use a weak coherent-state pulse instead and estimate the state-transfer fidelity for a single-photon input. Sections IV and V are respectively devoted to discussion and the conclusion. In Appendix A, we present the details of theory and numerical simulation results. In Appendices B and C, we present the details of the density matrix estimation. In Appendix D, we present the experimental information.

II. ATOM-PHOTON SWAP GATE

A. Setup

The setup for the present atom-photon SWAP gate is a common one in superconducting quantum computing: a superconducting atom is dispersively coupled to a microwave resonator, and transmission lines are attached to both of them (Fig. 1). One of the lines (port 2) is coupled to the atom and a microwave drive pulse, which transforms the *bare* states of the atom-resonator system to the *dressed* ones within the pulse duration, is applied through this line. The other line (port 1) is coupled to the resonator and a single microwave photon, which serves as a photon qubit, is input through this line synchronously with the drive pulse. The atom qubit is encoded on its ground and excited states, $|g\rangle$ and $|e\rangle$. The photon qubit is encoded on its two different

carrier frequencies, $|\omega_L\rangle$ and $|\omega_H\rangle$, where ω_L (ω_H) denotes the lower (higher) carrier frequency. The gate operation completes deterministically by bouncing the photon qubit.

The superconducting atom used in this experiment is a flux qubit containing three Josephson junctions in a loop [inset of Fig. 1(b)]. This flux qubit is always biased with a half-flux quantum and its transition frequencies are $\omega_{ge}/2\pi \sim 5.84$ GHz and $\omega_{ef}/2\pi \sim 14.5$ GHz, where $|g\rangle$, $|e\rangle$ and $|f\rangle$ respectively denote the ground, first excited, and second excited states. Note that the anharmonicity of flux qubits ($\omega_{ef} - \omega_{ge}$) is generally large and qubit manipulation by a short control pulse is possible. This atom is capacitively coupled at the end of a $\lambda/2$ resonator, whose resonant frequency is $\omega_r/2\pi = 10.258$ GHz when the atom is in the $|g\rangle$ state.

B. Working principle

Here, we outline the working principle of the gate. A detailed theoretical description is presented in Appendix A. We label the eigenstates of the atom-resonator system by $|a, n\rangle$, where $a = \{g, e\}$ and $n = \{0, 1, \dots\}$ respectively specify the atomic state and the resonator photon number. The atom-resonator system is in the dispersive coupling regime, and its eigenfrequencies are given by $\omega_{|g,n\rangle} = n\omega_r$ and $\omega_{|e,n\rangle} = \omega_{ge} + n(\omega_r - 2\chi)$, where ω_{ge} and ω_r are the renormalized frequencies of the atom and the resonator and χ is the dispersive frequency shift. In the present atom-photon gate, we use the lowest four levels of the atom-resonator system ($a = \{g, e\}$ and $n = \{0, 1\}$). The principal decay channel of this four-level system is the radiative decay of the resonator to port 1 with a rate of κ . Therefore, when the drive field is off, the radiative decay within this four-level system occurs vertically with κ [Fig. 2(a)].

During the interaction between the photon qubit and the atom-resonator system, we apply a microwave drive to the atom from port 2. This drive field hybridizes the lower two *bare* states $|g, 0\rangle$ and $|e, 0\rangle$ to form the *dressed* states $|\tilde{1}\rangle$ and $|\tilde{2}\rangle$. By switching on and off the drive field adiabatically, we can convert the bare and dressed states

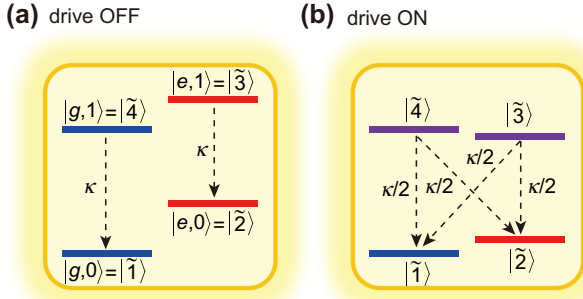


FIG. 2. Level structure of the atom-resonator system. (a) Bare states, where the drive field from port 2 is off. (b) Dressed states, where the drive field is on. Note that the energy diagram (b) is drawn in the frame rotating at the drive frequency ω_d .

deterministically as $|g, 0\rangle \leftrightarrow |\tilde{1}\rangle$ and $|e, 0\rangle \leftrightarrow |\tilde{2}\rangle$. Similarly, the higher two states are converted as $|e, 1\rangle \leftrightarrow |\tilde{3}\rangle$ and $|g, 1\rangle \leftrightarrow |\tilde{4}\rangle$. In addition to vertical decays ($|\tilde{3}\rangle \rightarrow |\tilde{2}\rangle$ and $|\tilde{4}\rangle \rightarrow |\tilde{1}\rangle$), oblique decays ($|\tilde{3}\rangle \rightarrow |\tilde{1}\rangle$ and $|\tilde{4}\rangle \rightarrow |\tilde{2}\rangle$) become allowed due to hybridization.

In particular, under a proper choice of the drive frequency and power, the four radiative decay rates take an identical value of $\kappa/2$ [Fig. 2(b)]. Then, the levels $|\tilde{1}\rangle$, $|\tilde{2}\rangle$, and $|\tilde{j}\rangle$ ($j = 3$ or 4) function as an “impedance-matched” Λ system [31,35]: if the system is in state $|\tilde{1}\rangle$ initially and a single photon with a frequency $\omega_{j1} = \omega_{\tilde{j}} - \omega_{\tilde{1}}$ is input from port 1, a Raman transition $|\tilde{1}\rangle \rightarrow |\tilde{j}\rangle \rightarrow |\tilde{2}\rangle$ is deterministically induced. As a result, the Λ system switches to state $|\tilde{2}\rangle$ and the input photon becomes down-converted to frequency ω_{j2} after reflection. In this study, we choose $j = 4$ and set $\omega_L = \omega_{42}$ and $\omega_H = \omega_{41}$ as the lower and higher carrier frequencies of the photon qubit. The time evolution of the atom and photon qubits is then written as $|\tilde{1}, \omega_H\rangle \rightarrow |\tilde{2}, \omega_L\rangle$. The inverse process, $|\tilde{2}, \omega_L\rangle \rightarrow |\tilde{1}, \omega_H\rangle$, is also deterministic. In contrast, for the initial states of $|\tilde{1}, \omega_L\rangle$ and $|\tilde{2}, \omega_H\rangle$, the input photon is perfectly reflected as it is without interacting with the Λ system, since the input photon is out of resonance of the Λ system. Namely, $|\tilde{1}, \omega_L\rangle \rightarrow |\tilde{1}, \omega_L\rangle$ and $|\tilde{2}, \omega_H\rangle \rightarrow |\tilde{2}, \omega_H\rangle$. These four time evolutions are summarized as

$$(\beta_1|\tilde{1}\rangle + \beta_2|\tilde{2}\rangle) \otimes (\gamma_1|\omega_L\rangle + \gamma_2|\omega_H\rangle) \rightarrow (\gamma_1|\tilde{1}\rangle + \gamma_2|\tilde{2}\rangle) \otimes (\beta_1|\omega_L\rangle + \beta_2|\omega_H\rangle), \quad (1)$$

where β_1, \dots, γ_2 are arbitrary coefficients satisfying $|\beta_1|^2 + |\beta_2|^2 = |\gamma_1|^2 + |\gamma_2|^2 = 1$.

Before and after the gate operation, we switch off the drive field. Then, the atom-resonator system returns to the bare state basis as $|\tilde{1}\rangle = |g, 0\rangle$ and $|\tilde{2}\rangle = |e, 0\rangle$. Omitting the resonator’s state, which is in the vacuum state at both

the initial and final moments, Eq. (1) is rewritten as

$$(\beta_1|g\rangle + \beta_2|e\rangle) \otimes (\gamma_1|\omega_L\rangle + \gamma_2|\omega_H\rangle) \rightarrow (\gamma_1|g\rangle + \gamma_2|e\rangle) \otimes (\beta_1|\omega_L\rangle + \beta_2|\omega_H\rangle). \quad (2)$$

This is a SWAP gate between the atom and photon qubits.

III. BIDIRECTIONAL QUBIT-STATE TRANSFER

In this section, we experimentally confirm the bidirectional state transfer between the atom and photon qubits. This should be done, in principle, by inputting a single-photon pulse from port 1 as the photon qubit. However, in this study, we use a weak coherent-state pulse (the mean photon number $|\alpha|^2 \ll 1$) instead and estimate the state-transfer fidelities for a single-photon input.

The photon-qubit pulse is dichromatic in general with carrier frequencies ω_L and ω_H and has a Gaussian temporal profile with a pulse length of $t_p = 100$ ns. This is long enough to satisfy the condition for a high-fidelity atom-photon gate, $t_p \gg 1/\kappa$, where κ is the resonator decay rate into port 1 (see Table III in Appendix D 2). If the initial states of the atom and photon qubits are $\beta_1|g\rangle + \beta_2|e\rangle$ and $\gamma_1|\omega_L\rangle + \gamma_2|\omega_H\rangle$, respectively, the initial state vector of the atom-photon system is written as

$$|\psi_i\rangle = (\beta_1|g\rangle + \beta_2|e\rangle) \otimes e^{-|\alpha|^2/2} [|0\rangle + \alpha(\gamma_1|\omega_L\rangle + \gamma_2|\omega_H\rangle) + \dots], \quad (3)$$

where α represents the dimensionless amplitude of the input coherent-state pulse, and the dots represent the multiphoton components in the pulse, which are negligible when $|\alpha|^2 \ll 1$. This state vector is rewritten as $|\psi_i\rangle = c_1|g, 0\rangle + c_2|e, 0\rangle + c_3|g, \omega_L\rangle + c_4|e, \omega_L\rangle + c_5|g, \omega_H\rangle + c_6|e, \omega_H\rangle + \dots$, where

$$(c_1, \dots, c_6) = e^{-|\alpha|^2/2} (\beta_1, \beta_2, \alpha\beta_1\gamma_1, \alpha\beta_2\gamma_1, \alpha\beta_1\gamma_2, \alpha\beta_2\gamma_2). \quad (4)$$

The present gate is completed by bouncing the photon qubit at the cavity attached to the atom qubit. The time evolution is given by Eq. (1) and results in the exchange of coefficients c_4 and c_5 . Thus, the final state vector is given by

$$|\psi_f\rangle = c_1|g, 0\rangle + c_2|e, 0\rangle + c_3|g, \omega_L\rangle + c_5|e, \omega_L\rangle + c_4|g, \omega_H\rangle + c_6|e, \omega_H\rangle + \dots. \quad (5)$$

A. Photon-to-atom state transfer

1. Procedures for density matrix estimation

In this subsection, we demonstrate the photon-to-atom state transfer. We denote the density matrix of the final atom qubit by $\hat{\rho}_a^{(c)}$, where the superscript (c)

implies that the input photon-qubit pulse is in a coherent state. The matrix element of $\hat{\rho}_a^{(c)}$ is given by $\rho_{a,mn}^{(c)} = \text{Tr}_p\{\langle m|\psi_f\rangle\langle\psi_f|n\rangle\}$, where $m, n (= g, e)$ specify the atomic state and Tr_p takes the trace over the photonic states. From Eq. (5), $\rho_{a,ee}^{(c)}$ and $\rho_{a,eg}^{(c)}$ are given, up to the second order in $|\alpha|$, by

$$\rho_{a,ee}^{(c)} \approx |\beta_2|^2 + |\alpha|^2(|\gamma_2|^2 - |\beta_2|^2), \quad (6)$$

$$\rho_{a,eg}^{(c)} \approx \beta_1^* \beta_2 + |\alpha|^2(\gamma_1^* \gamma_2 - \beta_1^* \beta_2). \quad (7)$$

On the other hand, our target quantity here is the density matrix $\hat{\rho}_a^{(s)}$ of the final atom qubit, assuming single-photon input. If the SWAP gate is performed with single-photon input, the final atomic state is $\gamma_1|g\rangle + \gamma_2|e\rangle$ [see Eq. (2)]. Therefore, $\rho_{a,ee}^{(s)} = |\gamma_2|^2$ and $\rho_{a,eg}^{(s)} = \gamma_1^* \gamma_2$.

Thus, we can reproduce the target density matrix $\hat{\rho}_a^{(s)}$ from the measurable one $\hat{\rho}_a^{(c)}$ by the following procedures. Setting the initial atomic state at $|g\rangle$ [namely, $(\beta_1, \beta_2) = (1, 0)$], we perform the atom-photon SWAP gate and measure the final atomic density matrix elements $\rho_{a,ee}^{(c)}$ and $\rho_{a,eg}^{(c)}$. Setting $(\beta_1, \beta_2) = (1, 0)$ in Eqs. (6) and (7), they are expected to be $\rho_{a,ee}^{(c)} = |\alpha|^2|\gamma_2|^2$ and $\rho_{a,eg}^{(c)} = |\alpha|^2\gamma_1^*\gamma_2$. Therefore, by varying the mean photon number $|\alpha|^2$ and measuring the slopes of these quantities, two of the target density matrix elements are estimated as

$$\rho_{a,ee}^{(s)} = \frac{d}{d|\alpha|^2} \rho_{a,ee}^{(c)}, \quad (8)$$

$$\rho_{a,eg}^{(s)} = \frac{d}{d|\alpha|^2} \rho_{a,eg}^{(c)}. \quad (9)$$

The other elements are determined as $\rho_{a,ge}^{(s)} = (\rho_{a,eg}^{(s)})^*$ and $\rho_{a,gg}^{(s)} = 1 - \rho_{a,ee}^{(s)}$.

2. Pulse sequence

The pulse sequence to measure the density matrix $\hat{\rho}_a^{(c)}$ of the final atom qubit is shown in Fig. 3(a). The measurement is composed of three steps.

(i) Initialization: we wait for complete de-excitation of the atom, applying no pulses.

(ii) SWAP gate: from port 2, we apply a drive pulse with a flat-top envelope at $\omega_d/2\pi = 5.785$ GHz to the atom to implement an *impedance-matched* Λ system [Fig. 2(b)]. Within the drive pulse duration, we input from port 1 the photon-qubit pulse with a Gaussian envelope, which is dichromatic ($\omega_L/2\pi = \omega_{A2}/2\pi = 10.208$ GHz and $\omega_H/2\pi = \omega_{A1}/2\pi = 10.266$ GHz) in general. Note that the photon-qubit pulse in Fig. 3(a) does not have a clear Gaussian envelope because of its dichromatic nature.

(iii) Tomography: we first apply a short control pulse (no pulse, π pulse, or four kinds of $\pi/2$ pulse) with a Gaussian envelope at $\omega_{ge}/2\pi = 5.839$ GHz to the atom and then

dispersively read out the atomic state with a rectangular pulse at $\omega_r/2\pi = 10.258$ GHz [42].

The bare qubit transition frequency is $\omega_{ge}/2\pi = 5.839$ GHz, whereas the dressed one is $(\omega_H - \omega_L + \omega_d)/2\pi = 5.843$ GHz. Thus, the qubit transition frequency increases by 4 MHz. Since we know the power and frequency of the applied drive field, we have access to the time-dependent frequency shift and, accordingly, to the accumulated phase difference due to the application of the drive pulse.

3. Results and discussion

The measured density matrix elements $\rho_{a,ee}^{(c)}$ and $\rho_{a,eg}^{(c)}$ of the final atom qubit are shown in Fig. 3(b), where the initial atom (photon) qubit is in the ground (equator) state, namely, $(\beta_1, \beta_2) = (1, 0)$ and $(\gamma_1, \gamma_2) = (1, e^{i\theta})/\sqrt{2}$. We observe that $\rho_{a,ee}^{(c)}$ is independent of the phase θ of the initial photon qubit and increases in proportion to $|\alpha|^2$, and that $\rho_{a,eg}^{(c)}$ is an oscillating function of θ and its amplitude grows by increasing $|\alpha|^2$. These observations are in qualitative accordance with Eqs. (6) and (7), which predict that $\rho_{a,ee}^{(c)} = |\alpha|^2/2$ and $\rho_{a,eg}^{(c)} = |\alpha|^2 e^{i\theta}/2$. These results indicate that the phase information of the initial photon qubit is successfully transferred to the final atom qubit.

In Fig. 3(c), we present the density matrix $\hat{\rho}_a^{(s)}$ of the final atom qubit, assuming single-photon input, estimated by the aforementioned procedures. More details on the estimation are presented in Appendix B. The initial photon qubit is in one of the six cardinal states [$|\omega_L\rangle$, $|\omega_H\rangle$, and $(|\omega_L\rangle + e^{in\pi/4}|\omega_H\rangle)/\sqrt{2}$ for $n = 0, \dots, 3$]. The agreement between the initial photon and final atom qubits is fairly good and the averaged fidelity for the six cardinal states reaches 0.826. The principal origin of the infidelity would be the short T_1 (about 0.9 μs) of the superconducting atom, which is comparable to the time required for the state tomography of the final atom qubit. An exceptionally high fidelity is attained when the initial photon qubit is in $|\omega_L\rangle$ [first panel of Fig. 3(c)]. This is because the atom remains in the ground state ($|g, 0\rangle \approx |\tilde{1}\rangle$) throughout the gate operation and is unaffected by the short T_1 .

B. Atom-to-photon state transfer

1. Procedures for density matrix estimation

In this subsection, we demonstrate the atom-to-photon state transfer. More concretely, from the amplitudes of the final photon-qubit pulse (after reflection in port 1) for the coherent-state input, we estimate the density matrix $\hat{\rho}_p^{(s)}$ of the final photon qubit, assuming single-photon input. The final amplitude $\xi(t)$ is given by $\xi(t) = \langle\psi_f|\hat{a}|\psi_f\rangle$, where \hat{a} is the annihilation operator for a propagating photon in port 1. Using Eq. (5), $\xi(t)$ is given, up to the first order in

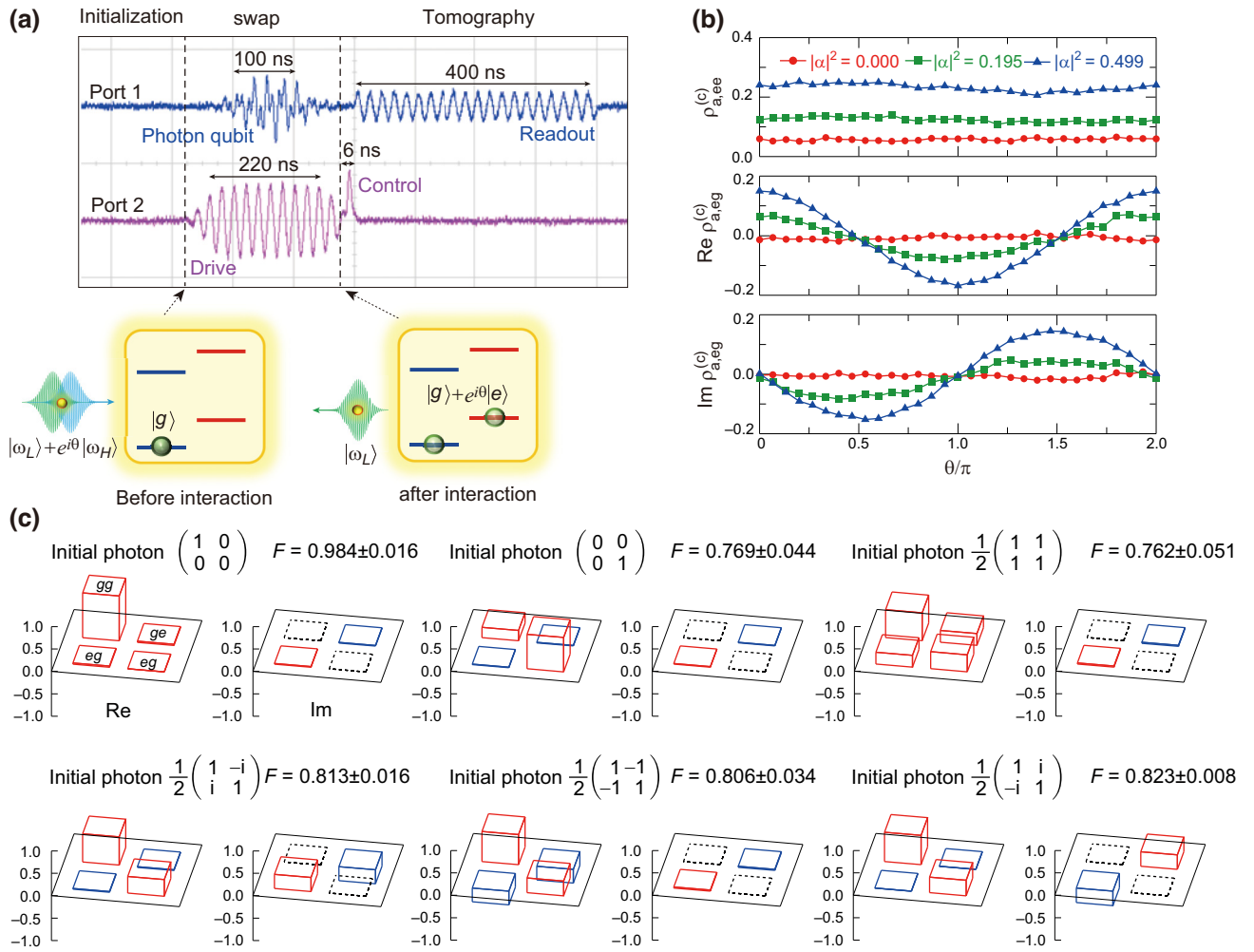


FIG. 3. Photon-to-atom state transfer. (a) Pulse sequence depicted in the intermediate frequencies and the energy diagrams before and after the SWAP gate. In the energy diagrams, the initial atom (photon) qubit is assumed to be in the polar (equator) state, namely, $(\beta_1, \beta_2) = (1, 0)$ and $(\gamma_1, \gamma_2) = (1, e^{i\theta})/\sqrt{2}$. The final photon is in $|\omega_L\rangle$, reflecting the initial atomic state $|g\rangle$. (b) Measured density matrix elements ($\rho_{a,ee}^{(c)}$, $\text{Re} \rho_{a,eg}^{(c)}$, $\text{Im} \rho_{a,eg}^{(c)}$) of the final atom qubit for the coherent-state input. The initial atom (photon) qubit is in the ground (equator) state, and the phase θ of the photon qubit is varied continuously. The mean photon number $|\alpha|^2$ in the photon-qubit pulse is indicated. (c) Estimated density matrix $\hat{\rho}_a^{(s)}$ of the final atom qubit, assuming single-photon input. Positive, negative, and zero matrix elements are drawn in red, blue, and black dotted lines, respectively. The fidelity between the initial photon and final atom qubits is indicated.

$|\alpha|$, by

$$\begin{aligned} \xi(t) = & \alpha(|\beta_1|^2 \gamma_1 + \beta_1 \beta_2^* \gamma_2) \psi_L(t) \\ & + \alpha(\beta_1^* \beta_2 \gamma_1 + |\beta_2|^2 \gamma_2) \psi_H(t), \end{aligned} \quad (10)$$

where $\psi_{L(H)}(t) = \langle 0 | \hat{a} | \omega_{L(H)} \rangle$ is the single-photon amplitude of the lower (higher) frequency component. When the initial photon-qubit pulse is monochromatic at ω_L , the final amplitude $\xi_L(t)$ is given, by putting $(\gamma_1, \gamma_2) = (1, 0)$ in Eq. (10), by

$$\xi_L(t) = \alpha |\beta_1|^2 \psi_L(t) + \alpha \beta_1^* \beta_2 \psi_H(t). \quad (11)$$

This equation implies that the initial monochromatic pulse may become dichromatic after reflection, depending on the initial atomic state. However, when the atom is in the ground state initially, the final pulse remains monochromatic at ω_L . We denote its amplitude by $\zeta_L(t)$. Setting $(\beta_1, \beta_2) = (1, 0)$ in Eq. (11), we have

$$\zeta_L(t) = \alpha \psi_L(t). \quad (12)$$

Similarly, when the initial pulse is monochromatic at ω_H , the final amplitude $\xi_H(t)$ is given by

$$\xi_H(t) = \alpha \beta_1 \beta_2^* \psi_L(t) + \alpha |\beta_2|^2 \psi_H(t). \quad (13)$$

Amplitude $\zeta_H(t)$ is the result of the initial atom being in the excited state. Setting $(\beta_1, \beta_2) = (0, 1)$ in Eq. (13), we have

$$\zeta_H(t) = \alpha\psi_H(t). \quad (14)$$

We denote the overlap integral between $\zeta_i(t)$ and $\xi_j(t)$ ($i, j = L, H$) by

$$\eta_{ij} = \int_{t_1}^{t_2} dt \zeta_i^*(t) \xi_j(t), \quad (15)$$

where the upper and lower bounds of integration, t_1 and t_2 , are chosen to completely cover the pulse durations of $\zeta_i(t)$ and $\xi_j(t)$. Since $\psi_L(t)$ and $\psi_H(t)$ are orthogonal to each other due to the different carrier frequencies, we obtain $\eta_{LL} = C|\alpha|^2|\beta_1|^2$, $\eta_{HH} = C|\alpha|^2|\beta_2|^2$, $\eta_{LH} = C|\alpha|^2\beta_1\beta_2^*$, and $\eta_{HL} = C|\alpha|^2\beta_1^*\beta_2$, where $C = \int dt |\psi_j(t)|^2$ ($j = L, H$).

On the other hand, our target quantity here is the density matrix $\hat{\rho}_p^{(s)}$ of the final photon qubit, assuming single-photon input. From the right-hand side of Eq. (2), we immediately have $\hat{\rho}_p^{(s)} = (\beta_1|\omega_L\rangle + \beta_2|\omega_H\rangle)(\beta_1^*\langle\omega_L| + \beta_2^*\langle\omega_H|)$. Therefore, the 2×2 matrix

$$\hat{\eta} = \frac{1}{\eta_{LL} + \eta_{HH}} \begin{pmatrix} \eta_{LL} & \eta_{LH} \\ \eta_{HL} & \eta_{HH} \end{pmatrix}, \quad (16)$$

is expected to be identical to the target density matrix $\hat{\rho}_p^{(s)}$.

Thus, we can construct the target density matrix $\hat{\rho}_p^{(s)}$ from the measured amplitudes of the final photon-qubit pulse by the following procedures. Preliminarily, setting the initial atom-qubit state at $|g\rangle$ ($|e\rangle$), we apply a monochromatic photon-qubit pulse at ω_L (ω_H) and measure the final amplitude $\zeta_L(t)$ [$\zeta_H(t)$]. Then, for an arbitrary initial atom-qubit state, we apply a monochromatic pulse at ω_L (ω_H) and measure the final amplitude $\xi_L(t)$ [$\xi_H(t)$]. We construct a 2×2 matrix $\hat{\eta}$ from the overlap integrals between these output amplitudes [Eqs. (15) and (16)]. Matrix $\hat{\eta}$ is identical to the target density matrix $\hat{\rho}_p^{(s)}$ in principle, but is non-Hermitian in practice (see Table II in Appendix C). We estimate a proper one by the protocol presented in Appendix C.

2. Pulse sequence

The pulse sequence to measure amplitude $\xi(t)$ of the final photon-qubit pulse is shown in Fig. 4(a). The measurement is composed of three steps.

(i) Initialization: we wait for complete de-excitation of the atom. We then apply a control pulse with a Gaussian envelope at $\omega_{ge}/2\pi = 5.835$ GHz from port 2 to the atom to prepare it in one of the six cardinal states.

(ii) SWAP gate: from port 2, we apply a drive pulse with a flat-top envelope at $\omega_d/2\pi = 5.775$ GHz to the atom

to constitute an *impedance-matched* Λ system [Fig. 2(b)]. Within the pulse duration, we input from port 1 a weak monochromatic (at $\omega_L/2\pi = 10.201$ GHz or $\omega_H/2\pi = 10.263$ GHz) photon-qubit pulse with a Gaussian envelope.

(iii) Measurement: we measure the amplitude of the reflected photon-qubit pulse in port 1, which is dichromatic in general. Note that ω_L and ω_H are slightly different from those in the ‘‘photon-to-atom’’ experiment, since the experiment was performed in the different cooling down of our dilution refrigerator (see Table III in Appendix D 2 for details on the experimental parameters).

All microwave pulses in Fig. 4(a) are generated by single-sideband modulation and are shown in the intermediate frequencies (IFs), similarly to those in Fig. 3(a). A carrier microwave at $\omega_c/2\pi = 10.308$ GHz and a Gaussian envelope with IF = $\delta\omega_H/2\pi = 0.045$ GHz ($\delta\omega_L/2\pi = 0.107$ GHz) are mixed by an in-phase and quadrature (IQ) mixer, obtaining the photon pulse with $\omega_H = \omega_c - \delta\omega_H$ ($\omega_L = \omega_c - \delta\omega_L$). The final photon-qubit pulses after reflection by the atom are measured by an analog-digital converter after down-conversion at ω_c in order to extract the signals at $\delta\omega_H$ ($\delta\omega_L$), as shown in the left panels of Figs. 4(b) and 4(c). The frequency-domain plots [right panels of Figs. 4(b) and 4(c)] are obtained by applying the fast Fourier transform to the time-domain plots.

3. Results and discussions

In Fig. 4(b), we plot the final amplitudes of the photon-qubit pulse in the time [$\xi_H(t)$, Eq. (13)] and frequency [$\xi_H(\omega)$, Fourier transform of $\xi_H(t)$] domains, fixing its initial frequency at ω_H and varying the initial atomic state. Predictions by Eq. (13) are as follows.

(i) Setting $(\beta_1, \beta_2) = (0, 1)$, we have $\xi_H(t) = \alpha\psi_H(t)$. Namely, when the atom is in the excited state initially, the final amplitude is monochromatic at ω_H , unchanged from the initial one.

(ii) Setting $(\beta_1, \beta_2) = (1, e^{i\theta})/\sqrt{2}$, we have $\xi_H(t) = (\alpha/2)[e^{-i\theta}\psi_L(t) + \psi_H(t)]$. Namely, when the atom is in the equator state initially, the final amplitude is dichromatic at ω_L and ω_H with equal magnitudes.

(iii) Setting $(\beta_1, \beta_2) = (1, 0)$, we have $\xi_H(t) = 0$. Namely, when the atom is in the ground state initially, the final amplitude vanishes.

We observe that the measured amplitudes in Fig. 4(b) are in qualitative agreement with these predictions. However, we also find discrepancies in these predictions, such as nonvanishing signal at ω_H for the initial atom in $|g\rangle$ and appearance of the ω_L component for the initial atom in $|e\rangle$. We attribute the principal reason for the former discrepancy to the imperfect constitution of an impedance-matched Λ system [namely, the difference in the $|4\rangle \rightarrow |\bar{1}\rangle$ and $|\bar{4}\rangle \rightarrow$

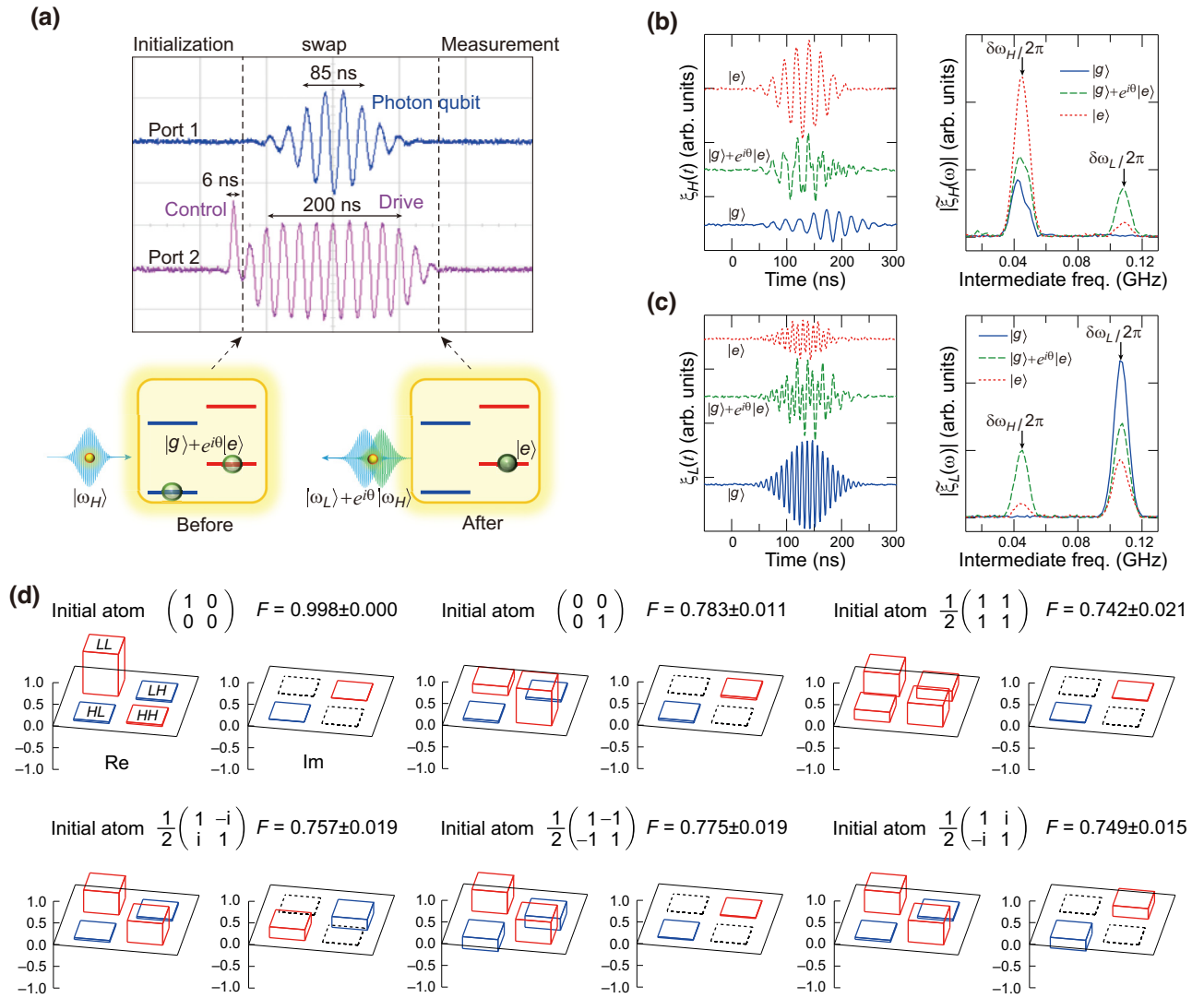


FIG. 4. Atom-to-photon state transfer. (a) Pulse sequence depicted in the intermediate frequencies and the energy diagrams before and after the SWAP gate. In the energy diagrams, the initial atom (photon) qubit is assumed to be in the equator (polar) state, namely, $(\beta_1, \beta_2) = (1, e^{i\theta})/\sqrt{2}$ and $(\gamma_1, \gamma_2) = (0, 1)$. (b) Measured amplitude of the output photon-qubit pulse for its initial frequency set at ω_H : time domain (left) and frequency domain (right). The initial atom-qubit state (ground, equator, or excited) is indicated. Since the four equator states yield similar spectra, only one of them is plotted. The mean photon number in the input pulse is $|\alpha|^2 = 0.101$. The time-domain amplitudes are measured by an analog-to-digital converter and are averaged over 1.5×10^4 times. (c) The same plots as (b) for the initial frequency of the photon-qubit pulse set at ω_L . (d) Estimated density matrix $\hat{\rho}_p^{(s)}$ of the final photon qubit, assuming single-photon input. Positive (negative) values are indicated by red (blue) bars. The fidelity between the initial atom and final photon qubits is indicated.

$|\tilde{2}\rangle$ decay rates in Fig. 2(b)] and the latter to the imperfect initialization of the atom qubit, both of which originate in the fluctuation in the transition frequency ω_{ge} of the superconducting atom. Note that the drastic attenuation of the final amplitude in (iii) does not mean the decrease of the reflected photon in port 1: the input photon is mostly down-converted to ω_L , but its amplitude is unobservable in this experiment due to the inelasticity of scattering. This quantum process (single-photon Raman interaction [32–39]) has been applied for single microwave-photon detection

[16,17]. Figure 4(c) shows the results for the initial frequency of the photon-qubit pulse tuned at ω_L . The results are contrastive to those in Fig. 4(b) and are in qualitative accordance with Eq. (11).

In Fig. 4(d), we present the density matrix $\hat{\rho}_p^{(s)}$ of the final photon qubit, assuming single-photon input, estimated by the aforementioned procedures. More details on the estimation are presented in Appendix C. The fidelity to the initial atom qubit, which is prepared to be in one of the six cardinal states, is fairly good and the average fidelity

reaches 0.801. An exceptionally high fidelity is attained when the initial atom is in $|g\rangle$ [first panel of Fig. 4(c)], because the atom remains in the ground state throughout the gate operation and is unaffected by the short T_1 (about 0.9 μs) of the superconducting atom. We observe that, when the initial atom qubit is in the equator states, the fidelities become substantially lower than those for the photon-to-atom state transfer [Fig. 3(c)]. Presently, we do not fully understand the reason for that. One possible reason might be that the amplitude of the frequency-converted component [ω_L (ω_H) component in the right panel of Fig. 4(b) [Fig. 4(c)]], which becomes observable only when the initial atom is in a superposition state, is more fragile against the pure dephasing than the amplitude of the unconverted component.

IV. DISCUSSION

Two comments are in order before concluding this paper. First, we comment on the implementation of the current scheme by mainstream superconducting qubits such as a transmon or a C -shunt flux qubit. A merit of using these mainstream qubits is that the lifetime of the atom becomes longer. This will substantially improve the fidelities in this experiment, since the principal origin of infidelities is the short lifetime of a flux qubit. On the other hand, the dispersive shifts of the mainstream qubits are generally smaller than the current one because of the smaller anharmonicity. Then, we need a smaller resonator linewidth κ and, accordingly, a longer photon-qubit pulse. This implies that the gate time would become longer in comparison with the current implementation.

For the case of a stronger photon-qubit pulse ($|\alpha|^2 \sim 1$), besides the zero- and one-photon components, multiphoton components become included in the pulse. Since the Λ system can interact with only a single photon simultaneously due to saturation, other photons in the pulse are reflected without swapping with the atom qubit. This results in a decrease in the SWAP probability per one photon and degrades the estimated fidelities.

V. CONCLUSION

In this work, we have confirmed the bidirectional state transfer between the atom and photon qubits. The photon qubit for this gate is an itinerant single-photon pulse, but we used a weak coherent-state pulse instead for demonstration. To confirm the photon-to-atom qubit transfer, we applied a monochromatic or dichromatic photon-qubit pulse, which corresponds to one of the six cardinal states of the photon qubit, to the dressed atom-resonator coupled system (impedance-matched Λ system). After reflection of this pulse, we performed a state tomography of the final atom qubit. From the dependencies of the density matrix elements on the mean input photon number, we constructed the density matrix of the final atom qubit,

assuming single-photon input. The fidelity to the initial photon qubit reaches 0.826 on average. On the other hand, to confirm the atom-to-photon qubit transfer, we prepared the initial atom qubit to be in one of the six cardinal states and applied a monochromatic photon-qubit pulse to the Λ system. From the measured amplitudes of the final photon-qubit pulse, we constructed the density matrix of the final photon qubit, assuming single-photon input. The fidelity to the initial atom qubit reaches 0.801 on average.

Although the state-transfer fidelities are still insufficient for practical application, the main origin of infidelities are the short lifetime of the superconducting atom, which can be overcome with the current qubit fabrication technology. We hope that the present atom-photon gate scheme, which is executable in a common setup (dispersively coupled qubit and cavity) in recent quantum processors, helps distributed quantum computing with superconducting qubits in the near future.

ACKNOWLEDGMENTS

The authors are grateful to T. Shitara, S. Masuda, and A. Noguchi for fruitful discussions. This work was supported by JST Moonshot R&D (JPMJMS2061, JPMJMS2062, JPMJMS2067), JSPS KAKENHI (22K03494), and JST PRESTO (JPMJPR1761).

APPENDIX A: THEORY OF THE ATOM-PHOTON (SWAP) $^\alpha$ GATE

1. Dressed states

In this appendix, we present a detailed theoretical description of the atom-photon gate (Fig. 1). We denote the drive frequency and amplitude by ω_d and Ω_d , respectively. In the frame rotating at ω_d , the Hamiltonian of the driven atom-resonator system is given, setting $\hbar = 1$, by

$$\begin{aligned} \hat{H}_{\text{ar}} = & \omega_r \hat{a}^\dagger \hat{a} \hat{\sigma} \hat{\sigma}^\dagger + [(\omega_a - \omega_d) + (\omega_r - 2\chi) \hat{a}^\dagger \hat{a}] \hat{\sigma}^\dagger \hat{\sigma} \\ & - \Omega_d (\hat{\sigma}^\dagger + \hat{\sigma}), \end{aligned} \quad (\text{A1})$$

where $\hat{\sigma} = |g\rangle\langle e|$ (\hat{a}) is the annihilation operator for the atom (resonator), ω_a (ω_r) is the resonance frequency of the atom (resonator), and χ is the dispersive shift.

The eigenstates of this driven Hamiltonian are referred to as the *dressed* states. In the present atom-photon gate, we use the lowest four dressed states. We choose the drive frequency ω_d within the range of $\omega_a - 2\chi < \omega_d < \omega_a$, where the microwave response of this four-level system becomes highly sensitive to the drive [35]. The four lowest

dressed states are given by

$$|\tilde{1}\rangle = \cos\theta_l|g, 0\rangle + \sin\theta_l|e, 0\rangle, \quad (\text{A2})$$

$$|\tilde{2}\rangle = -\sin\theta_l|g, 0\rangle + \cos\theta_l|e, 0\rangle, \quad (\text{A3})$$

$$|\tilde{3}\rangle = \cos\theta_h|e, 1\rangle + \sin\theta_h|g, 1\rangle, \quad (\text{A4})$$

$$|\tilde{4}\rangle = -\sin\theta_h|e, 1\rangle + \cos\theta_h|g, 1\rangle, \quad (\text{A5})$$

where

$$\theta_l = \frac{\arg[(\omega_a - \omega_d)/2 + i\Omega_d]}{2}, \quad (\text{A6})$$

$$\theta_h = \frac{\arg[(\omega_d - \omega_a + 2\chi)/2 + i\Omega_d]}{2}. \quad (\text{A7})$$

Their eigenenergies are given by

$$\omega_{1,2} = \frac{\omega_a - \omega_d}{2} \pm \sqrt{\left(\frac{\omega_a - \omega_d}{2}\right)^2 + \Omega_d^2}, \quad (\text{A8})$$

$$\omega_{3,4} = \omega_r - \frac{\omega_d - \omega_a + 2\chi}{2} \pm \sqrt{\left(\frac{\omega_d - \omega_a + 2\chi}{2}\right)^2 + \Omega_d^2}, \quad (\text{A9})$$

where the plus (minus) sign is taken for ω_2 and ω_4 (ω_1 and ω_3). When the drive is off ($\Omega_d = 0$), the dressed states $|\tilde{1}\rangle$, $|\tilde{2}\rangle$, $|\tilde{3}\rangle$, and $|\tilde{4}\rangle$ respectively reduce to the *bare* states $|g, 0\rangle$, $|e, 0\rangle$, $|e, 1\rangle$, and $|g, 1\rangle$. By smoothly changing the drive amplitude (about 40 ns; see Appendix A 3 b below), we can adiabatically switch the bare and dressed states.

2. Single-photon response

In this subsection, we discuss the interaction between the atom and photon qubits. We derive Eq. (1) in the main text, which holds in the long-pulse limit.

a. Heisenberg equations in the dressed-state basis

Denoting the decay rate of the resonator to port 1 by κ , the Hamiltonian to describe the resonator-waveguide interaction is given by

$$\hat{H}_{\text{rw}} = \int dk [k\hat{a}_k^\dagger\hat{a}_k + \sqrt{\kappa/2\pi}(\hat{a}^\dagger\hat{a}_k + \hat{a}_k^\dagger\hat{a})], \quad (\text{A10})$$

where \hat{a}_k annihilates an itinerant photon in port 1 with wave number k . Switching to the dressed-state basis [Eqs. (A2)–(A5)], the overall Hamiltonian $\hat{H} = \hat{H}_{\text{ar}} + \hat{H}_{\text{rw}}$ is

rewritten as

$$\hat{H} = \sum_j \omega_j \hat{\sigma}_{jj} + \int dk \times \left[k\hat{a}_k^\dagger\hat{a}_k + \sum_{ij} (\eta_{ji}\hat{\sigma}_{ji}\hat{a}_k + \eta_{ji}^*\hat{a}_k^\dagger\hat{\sigma}_{ij})/\sqrt{2\pi} \right], \quad (\text{A11})$$

where the indices run over $i, j = 1, \dots, 4$ and $\hat{\sigma}_{ji} = |\tilde{j}\rangle\langle\tilde{i}|$. The coefficient η_{ji} is defined by $\eta_{ji} = \sqrt{\kappa}\langle\tilde{j}|\hat{a}^\dagger|\tilde{i}\rangle$. More concretely, it is given by

$$\eta_{ji} = \sqrt{\kappa} \times \begin{cases} \cos\theta_l, & (j, i) = (3, 2) \text{ or } (4, 1), \\ (-1)^{j+1} \sin\theta_l, & (j, i) = (3, 1) \text{ or } (4, 2), \\ 0, & \text{otherwise,} \end{cases} \quad (\text{A12})$$

$$\theta_l = \theta_l + \theta_h. \quad (\text{A13})$$

We introduce the real-space representation of the field operator by $\hat{b}_r = (2\pi)^{-1/2} \int dk e^{ikr}\hat{a}_k$. In this representation, the $r < 0$ ($r > 0$) region corresponds to the incoming (outgoing) field. From Eq. (A11), we can rigorously derive the input-output relation

$$\hat{b}_r(t) = \hat{b}_{r-t}(0) - i\theta(r)\theta(t-r) \sum_{ij} \eta_{ji}^*\hat{\sigma}_{ij}(t-r), \quad (\text{A14})$$

where $\theta(r)$ is the Heaviside step function. From Eq. (A11), we can also derive the Heisenberg equations for $\hat{\sigma}_{ji}$. Those for the relevant operators in this subsection are

$$\begin{aligned} \frac{d}{dt}\hat{\sigma}_{1n} &= (-i\omega_{n1} - \kappa/2)\hat{\sigma}_{1n} + i[\eta_{n1}(\hat{\sigma}_{nn} - \hat{\sigma}_{11}) - \eta_{n2}\hat{\sigma}_{12} \\ &\quad + \eta_{\bar{n}1}\hat{\sigma}_{\bar{n}\bar{n}}]\hat{b}_{-t}(0), \end{aligned} \quad (\text{A15})$$

$$\begin{aligned} \frac{d}{dt}\hat{\sigma}_{2n} &= (-i\omega_{n2} - \kappa/2)\hat{\sigma}_{2n} + i[\eta_{n2}(\hat{\sigma}_{nn} - \hat{\sigma}_{22}) - \eta_{n1}\hat{\sigma}_{21} \\ &\quad + \eta_{\bar{n}2}\hat{\sigma}_{\bar{n}\bar{n}}]\hat{b}_{-t}(0), \end{aligned} \quad (\text{A16})$$

where $(n, \bar{n}) = (3, 4)$ or $(4, 3)$ and $\omega_{ji} = \omega_j - \omega_i$.

b. Wave functions of the initial and final photon qubits

In this subsection, we derive the formulas that determine the wave functions of the final photon. For the moment, we focus on the following case: the atom is in state $|\tilde{1}\rangle$ and a single photon with wave function $f(r)$ is input at the initial moment ($t = 0$). The initial state vector is then written as

$$|\phi(0)\rangle = \int dr f(r)\hat{b}_r^\dagger|\tilde{1}, \mathbf{v}\rangle, \quad (\text{A17})$$

where $|\mathbf{v}\rangle$ represents the vacuum state of the waveguide (port 1). We denote the final moment of this atom-photon

gate by t . The initial and final state vectors are connected by the unitary time evolution, $|\phi(t)\rangle = e^{-i\hat{H}t}|\phi(0)\rangle$. The final state vector is written as

$$|\phi(t)\rangle = e^{-i\omega_1 t} \int dr g_{11}(r, t) \hat{b}_r^\dagger |\tilde{1}, \mathbf{v}\rangle + e^{-i\omega_2 t} \int dr g_{12}(r, t) \hat{b}_r^\dagger |\tilde{2}, \mathbf{v}\rangle, \quad (\text{A18})$$

where $g_{11}(r, t)$ and $g_{12}(r, t)$ are the output photon wave functions after reflection. Note that the natural time evolution of the dressed state ($e^{-i\omega_j t}$) is separated.

From Eq. (A18), we have $g_{11}(r, t) = e^{i\omega_1 t} \langle \tilde{1}, \mathbf{v} | \hat{b}_r | \phi(t) \rangle = \langle \tilde{1}, \mathbf{v} | \hat{b}_r(t) | \phi(0) \rangle$. Similarly, $g_{12}(r, t) = \langle \tilde{2}, \mathbf{v} | \hat{b}_r(t) | \phi(0) \rangle$. Substituting Eq. (A14) into these equations, we obtain

$$g_{11}(r, t) = f(r-t) - i \sum_{n=3,4} \eta_{n1}^* s_{1n}(t-r), \quad (\text{A19})$$

$$g_{12}(r, t) = -i \sum_{n=3,4} \eta_{n2}^* s_{2n}(t-r), \quad (\text{A20})$$

where $s_{1n}(t)$ and $s_{2n}(t)$ are defined by $s_{1n}(t) = \langle \tilde{1}, \mathbf{v} | \hat{\sigma}_{1n}(t) | \phi(0) \rangle$ and $s_{2n}(t) = \langle \tilde{2}, \mathbf{v} | \hat{\sigma}_{2n}(t) | \phi(0) \rangle$. Their equations of motion are given, remembering that $\hat{b}_{-l}(0) | \phi(0) \rangle = f(-t) | \tilde{1}, \mathbf{v} \rangle$ and that $|\tilde{1}, \mathbf{v}\rangle$ ($|\tilde{2}, \mathbf{v}\rangle$) is an eigenstate of \hat{H} with eigenfrequency ω_1 (ω_2), by

$$\frac{d}{dt} s_{1n} = (-i\omega_{n1} - \kappa/2) s_{1n} - i\eta_{n1} f(-t), \quad (\text{A21})$$

$$\frac{d}{dt} s_{2n} = (-i\omega_{n2} - \kappa/2) s_{2n} - i\eta_{n1} f(-t) e^{i\omega_{21} t}. \quad (\text{A22})$$

c. Adiabatic solution in the long-pulse limit

We denote the central frequency of the input photon by ω . Namely, $f(-t) \sim e^{-i\omega t}$ and $f(-t) e^{i\omega_{21} t} \sim e^{-i(\omega - \omega_{21})t}$. In the long-pulse limit, where the pulse length of the input photon is much longer than κ^{-1} , Eqs. (A21) and (A22) are adiabatically solved as

$$s_{1n}(t) = \frac{-i\eta_{n1}}{\kappa/2 - i(\omega - \omega_{n1})} f(-t), \quad (\text{A23})$$

$$s_{2n}(t) = s_{1n}(t) e^{i\omega_{21} t}. \quad (\text{A24})$$

From Eqs. (A19), (A20), (A23), and (A24), the output wave functions g_{11} and g_{12} are recast in the following

forms:

$$g_{11}(r, t) = \xi_{11}(\omega) f(r-t), \quad (\text{A25})$$

$$g_{12}(r, t) = \xi_{12}(\omega) f(r-t) e^{-i\omega_{21}(r-t)}, \quad (\text{A26})$$

$$\xi_{11}(\omega) = 1 - \frac{\kappa \sin^2 \theta_t}{\kappa/2 - i(\omega - \omega_{31})} - \frac{\kappa \cos^2 \theta_t}{\kappa/2 - i(\omega - \omega_{41})}, \quad (\text{A27})$$

$$\xi_{12}(\omega) = -\frac{\kappa \cos \theta_t \sin \theta_t}{\kappa/2 - i(\omega - \omega_{31})} + \frac{\kappa \cos \theta_t \sin \theta_t}{\kappa/2 - i(\omega - \omega_{41})}. \quad (\text{A28})$$

The central frequency of g_{11} is unchanged from the input. In contrast, due to the phase factor $e^{-i\omega_{21}(r-t)}$ in Eq. (A26), the central frequency of g_{12} is red shifted from the input by ω_{21} . The envelopes of g_{11} and g_{12} are unchanged from the input.

Repeating the same arguments, the output wave functions g_{21} and g_{22} starting from the initial atom-qubit state $|\tilde{2}\rangle$ are obtained as

$$g_{21}(r, t) = \xi_{21}(\omega) f(r-t) e^{i\omega_{21}(r-t)}, \quad (\text{A29})$$

$$g_{22}(r, t) = \xi_{22}(\omega) f(r-t), \quad (\text{A30})$$

$$\xi_{21}(\omega) = -\frac{\kappa \cos \theta_t \sin \theta_t}{\kappa/2 - i(\omega - \omega_{32})} + \frac{\kappa \cos \theta_t \sin \theta_t}{\kappa/2 - i(\omega - \omega_{42})}, \quad (\text{A31})$$

$$\xi_{22}(\omega) = 1 - \frac{\kappa \cos^2 \theta_t}{\kappa/2 - i(\omega - \omega_{32})} - \frac{\kappa \sin^2 \theta_t}{\kappa/2 - i(\omega - \omega_{42})}. \quad (\text{A32})$$

Note that the central frequency of g_{21} is blue shifted from the input by ω_{21} , whereas the central frequency of g_{22} remains unchanged.

d. SWAP gate

From the above arguments, the time evolution of the atom and photon qubits is written, in the long-pulse limit, as

$$|\tilde{1}, \omega\rangle \rightarrow \xi_{11}(\omega) |\tilde{1}, \omega\rangle + \xi_{12}(\omega) |\tilde{2}, \omega - \omega_{21}\rangle, \quad (\text{A33})$$

$$|\tilde{2}, \omega\rangle \rightarrow \xi_{21}(\omega) |\tilde{1}, \omega + \omega_{21}\rangle + \xi_{22}(\omega) |\tilde{2}, \omega\rangle. \quad (\text{A34})$$

Note the probability conservation, $|\xi_{11}|^2 + |\xi_{12}|^2 = |\xi_{21}|^2 + |\xi_{22}|^2 = 1$.

Here, we consider the specific case of an *impedance-matched* Λ system ($\theta_t = \pi/4$), which is feasible by adjusting the drive frequency and amplitude. In this case, the four decay rates within this four-level system become identical [see Fig. 2(b)]. Throughout this study, we choose state $|\tilde{4}\rangle$ as the excited state of the Λ system. Therefore, the lower

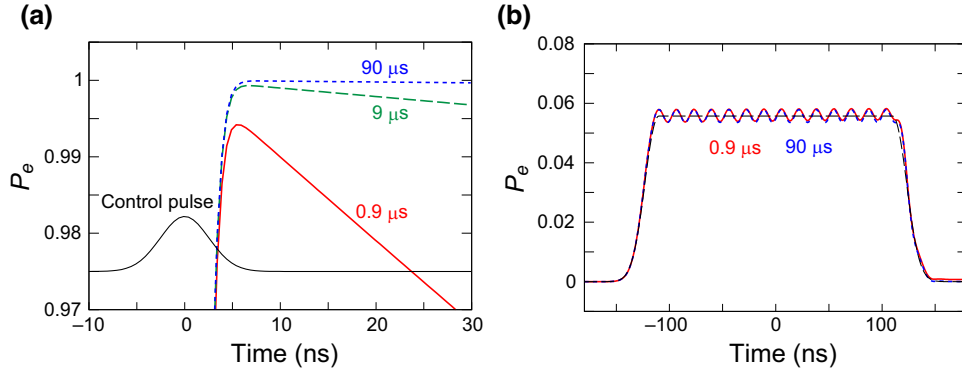


FIG. 5. Time evolution of the atomic excitation probability, $P_e = \langle \hat{\sigma}^\dagger \hat{\sigma} \rangle$, induced by the (a) control and (b) drive pulses. In (a), a π pulse is assumed as the control pulse and the atomic lifetime T_1 is varied: $T_1 = 0.9 \mu\text{s}$ (red solid), $9 \mu\text{s}$ (green dashed), and $90 \mu\text{s}$ (blue dotted). The thin line represents the control pulse shape. In (b), the results for $T_1 = 0.9 \mu\text{s}$ (red solid) and $90 \mu\text{s}$ (blue dotted) are mostly overlapping. The thin dashed line represents the adiabatic limit.

and higher carrier frequencies of the photon qubit are $\omega_L = \omega_{42}$ and $\omega_H = \omega_{41}$, respectively. We also set the linewidths of these transitions, which are of the order of κ , to be small enough that ω_L and ω_H do not induce nontarget transitions. We then observe that, for example, $\xi_{21}(\omega_L) \approx 1$ and $\xi_{22}(\omega_L) \approx 0$ and therefore that $|\tilde{2}, \omega_L\rangle \rightarrow |1, \omega_H\rangle$. Similarly, $|1, \omega_L\rangle \rightarrow |1, \omega_L\rangle$, $|1, \omega_H\rangle \rightarrow |2, \omega_L\rangle$, and $|2, \omega_H\rangle \rightarrow |2, \omega_H\rangle$. These four time evolutions are rewritten as Eq. (1) of the main text.

3. Numerical simulation

In the previous subsection, we analytically derived the formula for the single-photon response, assuming an infinite lifetime of the atom. Here, we present the results of numerical simulation, taking into account the finite lifetime of the atom ($T_1 \sim 0.9 \mu\text{s}$).

a. Control pulse

We first evaluate the fidelities of the single-qubit gates implemented by the control pulse applied to the atom

[Figs. 3(a) and 4(a)]. The control pulse is a short pulse in resonance with the atom. It has the Gaussian profile

$$f_c(t) = E_c e^{-i(\omega_c t - \theta_c)} \times 2^{-4t^2/l_c^2}, \quad (\text{A35})$$

where ω_c , l_c , θ_c , and E_c are the central frequency, length (in time), phase, and maximum amplitude of the pulse. The former two parameters are set at $\omega_c = \omega_a = 2\pi \times 5.839 \text{ GHz}$ and $l_c = 6 \text{ ns}$. The latter two parameters, E_c and θ_c , depend on the gate type.

Note that we can use a short control pulse in the present experiments. This is because the atom is implemented by a flux qubit, which behaves as an ideal two-level atom due to its large anharmonicity in contrast with a transmon qubit.

In Fig. 5(a), the time evolution of the excitation probability of the atom ($P_e = \langle \hat{\sigma}^\dagger \hat{\sigma} \rangle$) under irradiation of a π pulse is plotted, varying T_1 of the atom. The gate fidelity (P_e after π -pulse irradiation) improves monotonously for better T_1 . In the actual experiments ($T_1 \sim 0.9 \mu\text{s}$), the gate fidelity amounts to about 0.994. The 0.6% loss can be

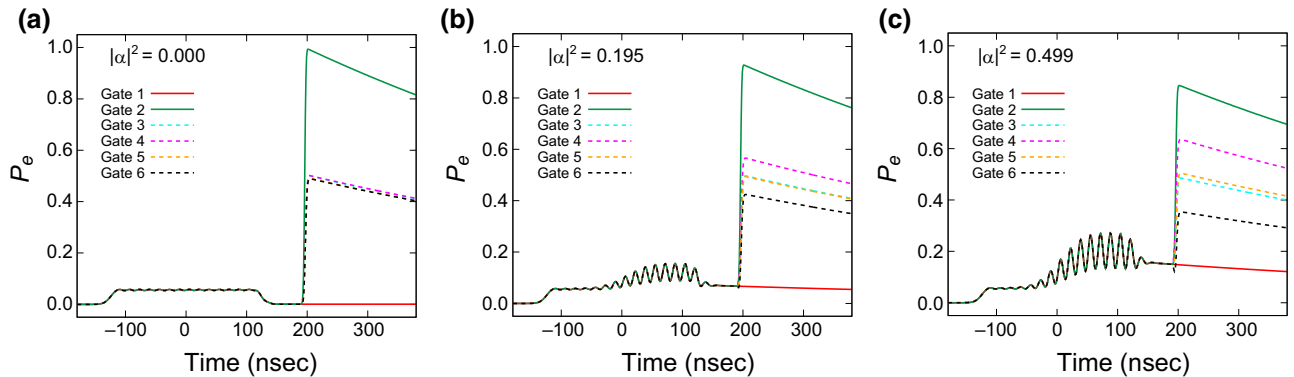


FIG. 6. Time evolution of the atomic excitation probability, $P_e = \langle \hat{\sigma}^\dagger \hat{\sigma} \rangle$, in the photon-to-atom transfer experiment. The initial photon-qubit state is $(|\omega_L\rangle - i|\omega_H\rangle)/\sqrt{2}$. The mean photon number $|\alpha|^2$ is 0 in (a), 0.195 in (b), and 0.499 in (c).

TABLE I. Estimation of the final atom-qubit state in the photon-to-atom transfer experiment. The initial photon-qubit state is $|\psi_p\rangle = (|\omega_L\rangle - i|\omega_H\rangle)/\sqrt{2}$. The state-transfer fidelity is $\langle\psi_p|\hat{\rho}_a^{(s)}|\psi_p\rangle = (1 + b_y)/2 = 0.823 \pm 0.008$.

$ \alpha ^2$	\tilde{p}_1	\tilde{p}_2	\tilde{p}_3	\tilde{p}_4	\tilde{p}_5	\tilde{p}_6	a_x	a_y	a_z	b_x	b_y	b_z
0.0000	0.0371	0.9226	0.4953	0.4965	0.4812	0.4821	0.0141	0.0144	-0.8855	-0.0032 ± 0.0351	0.6459 ± 0.0163	-0.3073 ± 0.0174
0.1950	0.0721	0.8306	0.4795	0.5452	0.4823	0.4124	-0.0028	0.1328	-0.7585			
0.4992	0.1950	0.7358	0.4800	0.6442	0.4697	0.3084	0.0103	0.3358	-0.5408			

understood as the decay during the pulse duration ($l_c/T_1 \sim 0.67\%$).

b. Drive pulse

Next, we investigate the dynamics induced by the drive pulse applied to the atom [Figs. 3(a) and 4(a)]. Its pulse profile is given by

$$f_d(t) = E_d e^{-i\omega_d t} \times \begin{cases} 1, & |t| < l_{d1}/2, \\ 2^{-4(|t-l_{d1}/2|^2/l_{d2}),} & \text{otherwise,} \end{cases} \quad (\text{A36})$$

where ω_d , l_{d1} , l_{d2} , and E_d respectively represent the central frequency, duration, rise or fall time, and the maximum amplitude. The former three parameters are set at $\omega_d/2\pi = 5.785$ GHz (which satisfies $\omega_a - 2\chi < \omega_d < \omega_a$ [35]), $l_{d1} = 220$ ns, and $l_{d2} = 40$ ns. The maximum amplitude E_d is adjusted to form an impedance-matched Λ system.

In Fig. 5(b), the time evolution of P_e under irradiation of the drive pulse is plotted. Although the system remains in state $|1\rangle$ during the drive duration, P_e slightly increases ($P_e \approx 0.056$) due to the formation of the dressed states. The thin dotted line shows the result in the adiabatic limit, namely, the value of $|\langle e, 0|\tilde{1}\rangle|^2$ at each moment. We observe a good agreement between the actual time evolution and the adiabatic limit: the residual excitation probability after the drive pulse duration ($t = 150$ nsec) is as small as 0.084%. This indicates that the rise or fall time of the drive pulse (40 nsec) is long enough to suppress the nonadiabatic transition.

c. Photon-qubit pulse

Synchronously to the drive pulse, we also apply the photon-qubit pulse to the resonator from port 1 [Figs. 3(a) and 4(a)]. It is dichromatic in general and has the Gaussian profile

$$f_p(t) = \alpha C [\cos(\theta_p/2) e^{-i\omega_L t} + \sin(\theta_p/2) e^{-i(\omega_H t - \phi_p)}] \times 2^{-4t^2/l_p^2}, \quad (\text{A37})$$

where l_p and α respectively represent the length and complex amplitude of the pulse. The normalization constant C is chosen as $C = (8 \ln 2/\pi l_p^2)^{1/4}$, so that $|\alpha|^2$ represents the mean photon number in this pulse, namely, $\int dt |f_p(t)|^2 = |\alpha|^2$. We respectively represent by θ_p and ϕ_p the polar and azimuthal angles of the qubit state on the Bloch sphere, which are chosen according to the photon-qubit state.

In Fig. 6, we present the numerical simulation results for the photon-to-atom transfer experiment. We first apply the drive and photon-qubit pulses synchronously ($-150 \lesssim t \lesssim 150$ ns). The photon-qubit state is fixed here at $(|\omega_L\rangle - i|\omega_H\rangle)/\sqrt{2}$ [$\theta_p = \pi/2$ and $\phi_p = -\pi/2$ in Eq. (A37)] and

three values of $|\alpha|^2$ are employed. We then apply the control pulse ($t \sim 200$ ns) to perform one of the six kinds of one-qubit gates [Eq. (B1) below] to the atom qubit. More concretely, we apply no pulse in gate 1, a π pulse in gate 2, and $\pi/2$ pulses in gates 3–6. After the application of the control pulse, we measure the atomic excitation probability P_e . The duration of the readout pulse is about 400 ns, but discrimination of the atomic state is done by integrating the readout pulse for 100 ns after the transient response time of 70 ns. Therefore, the measured excitation probability [shown in Table I] is expected to be P_e at $t \sim 300$ ns. For the case of $|\alpha|^2 = 0.195$ for example, the simulated excitation probabilities are $(\tilde{p}_1, \tilde{p}_2, \tilde{p}_3, \tilde{p}_4, \tilde{p}_5, \tilde{p}_6) = (0.0587, 0.8328, 0.4454, 0.5013, 0.4454, 0.3895)$, which are in fair agreement with the measured ones (the second line of Table I).

d. Origin of infidelity

Here, we discuss the origin of infidelity and potential improvement by numerical simulation. We focus on the fidelity of photon-to-atom transfer experiment for the initial photon-qubit state of $(|\omega_L\rangle - i|\omega_H\rangle)/\sqrt{2}$ for example.

When we evaluate the fidelity by numerical simulation with the parameter values in the actual experiment, the fidelity is as low as 0.741. (i) One major origin of infidelity is insufficient weakness of the photon-qubit pulse ($|\alpha|^2 \gtrsim 0.2$) in the present experiment. If we could use

a sufficiently weak pulse ($|\alpha|^2 \lesssim 0.05$) and estimate the fidelity for a single-photon input more rigorously, the fidelity reaches 0.839. (ii) Leaving the system parameters unchanged and optimizing the photon-qubit pulse ($\omega_L/2\pi = 10.204$ GHz, $\omega_H/2\pi = 10.267$ GHz, and pulse length 85 ns), this fidelity is slightly improved to be 0.849. This fact indicates a merit of the present scheme, namely, insensitivity to the pulse shape of the photon qubit. (iii) The other major origin of infidelity is the short lifetime of the atom qubit ($T_1 = 0.9$ μ s). Assuming a better atom qubit ($T_1 = 90$ μ s) and optimizing the lengths of the drive and photon-qubit pulses (575 and 261 ns, respectively), the fidelity reaches 0.975. (iv) The residual infidelity is due to the existence of dressed state $|\tilde{3}\rangle$. Further improvement could be done by increasing the dispersive frequency shift χ .

APPENDIX B: DENSITY MATRIX ESTIMATION: PHOTON TO ATOM

Here, we present the details of the density matrix estimation for the photon-to-atom state transfer [Fig. 3(c)]. We first discuss how to determine the density matrix $\hat{\rho}_a^{(c)}$ of the final atom qubit from the measurement data. In the tomography stage of Fig. 3(a), we first perform one of the six kinds of one-qubit gates to the atom. The unitary matrices corresponding to these gates are

$$\hat{U}_j = \begin{cases} \hat{I}, & j = 1, \\ \hat{\sigma}_x, & j = 2, \\ \left[\hat{I} - i \cos\left(\frac{j\pi}{2}\right) \hat{\sigma}_x - i \sin\left(\frac{j\pi}{2}\right) \hat{\sigma}_y \right] / \sqrt{2}, & j = 3, \dots, 6. \end{cases} \quad (\text{B1})$$

We measure the excitation probability of the atom by the dispersive readout. We denote the *measured* probability after the j th gate by \tilde{p}_j . We estimate the atomic density matrix $\hat{\rho}_a^{(c)}$ from the measurement data set $(\tilde{p}_1, \dots, \tilde{p}_6)$.

We parameterize $\hat{\rho}_a^{(c)}$ as

$$\hat{\rho}_a^{(c)} = (\hat{I} + a_x \hat{\sigma}_x + a_y \hat{\sigma}_y + a_z \hat{\sigma}_z) / 2, \quad (\text{B2})$$

where a_x , a_y , and a_z are the Bloch vector components, which are real and satisfy $a_x^2 + a_y^2 + a_z^2 \leq 1$. The *expected* excitation probability p_j after the j th gate is given by $p_j = \text{Tr}\{(\hat{I} + \hat{\sigma}_z) \hat{U}_j \hat{\rho}_a^{(c)} \hat{U}_j^\dagger\} / 2$. From Eqs. (B1) and (B2), this probability reduces to $p_1 = (1 + a_z)/2$, $p_2 = (1 - a_z)/2$, $p_3 = (1 + a_x)/2$, $p_4 = (1 + a_y)/2$, $p_5 = (1 - a_x)/2$, and $p_6 = (1 - a_y)/2$. We determine the parameters a_x , a_y , and a_z so as to minimize the sum of squared errors, $S(a_x, a_y, a_z) = \sum_{j=1}^6 (p_j - \tilde{p}_j)^2$. This is rewritten as $S(a_x, a_y, a_z) = (a_x - \bar{a}_x)^2 / 4 +$

$(a_y - \bar{a}_y)^2 / 4 + (a_z - \bar{a}_z)^2 / 4 + \dots$, where

$$\bar{a}_x = \tilde{p}_3 - \tilde{p}_5, \quad (\text{B3})$$

$$\bar{a}_y = \tilde{p}_4 - \tilde{p}_6, \quad (\text{B4})$$

$$\bar{a}_z = \tilde{p}_1 - \tilde{p}_2. \quad (\text{B5})$$

Therefore, if point $P(\bar{a}_x, \bar{a}_y, \bar{a}_z)$ is inside of the unit sphere, S is minimized at this point. In contrast, if point P is out of the unit sphere, S is minimized at the projection of point P to the unit-sphere surface in the radial direction. Therefore,

$$(a_x, a_y, a_z) = \frac{(\bar{a}_x, \bar{a}_y, \bar{a}_z)}{\max(1, \sqrt{\bar{a}_x^2 + \bar{a}_y^2 + \bar{a}_z^2})}. \quad (\text{B6})$$

Next, we discuss the estimation of the atomic density matrix $\hat{\rho}_a^{(s)}$ for the single-photon input from the one $\hat{\rho}_a^{(c)}$

for the coherent-state input. Similarly to Eq. (B2), we parameterize the target density matrix as

$$\hat{\rho}_a^{(s)} = (\hat{I} + b_x \hat{\sigma}_x + b_y \hat{\sigma}_y + b_z \hat{\sigma}_z)/2. \quad (\text{B7})$$

Then, From Eqs. (8) and (9), we obtain

$$b_j = \begin{cases} \frac{da_j}{d|\alpha|^2}, & j = x, y, \\ \frac{da_j}{d|\alpha|^2} - 1, & j = z. \end{cases} \quad (\text{B8})$$

Therefore, we can estimate b_j from the dependence of a_j on the mean input photon number $|\alpha|^2$. We estimate b_j by assuming a linear dependence and employing the least square method. In Table I, setting the initial photon qubit at $|\psi_p\rangle = (|\omega_L\rangle - i|\omega_H\rangle)/\sqrt{2}$ for example, we present the measurement data set $(\tilde{p}_1, \dots, \tilde{p}_6)$ and the estimated Bloch vector components, (a_x, a_y, a_z) and (b_x, b_y, b_z) .

APPENDIX C: DENSITY MATRIX ESTIMATION: ATOM TO PHOTON

Here, we present the details of the density matrix estimation for the atom-to-photon state transfer [Fig. 4(d)]. According to the arguments in Sec. III B, matrix $\hat{\eta}$ constructed directly from the experimental data [Eqs. (15) and (16)] is, in principle, identical to the target density matrix $\hat{\rho}_p^{(s)}$. However, as we observe in Table II, $\hat{\eta}$ is non-Hermitic in practice. We therefore estimate a proper density matrix $\hat{\rho}_p^{(s)}$ from $\hat{\eta}$ by the following procedures.

Similarly to Eq. (B2), we parameterize the proper density matrix as

$$\hat{\rho}_p^{(s)} = (\hat{I} + c_x \hat{\sigma}_x + c_y \hat{\sigma}_y + c_z \hat{\sigma}_z)/2, \quad (\text{C1})$$

where $c_x, c_y,$ and c_z are real and satisfy $c_x^2 + c_y^2 + c_z^2 \leq 1$. We choose $c_x, c_y,$ and c_z so as to minimize the distance L between $\hat{\eta}$ and $\hat{\rho}_p^{(s)}$, which we quantify by

$$L(c_x, c_y, c_z) = \sum_{j=x,y,z} |\langle \hat{\sigma}_j \rangle_\eta - \langle \hat{\sigma}_j \rangle_\rho|^2, \quad (\text{C2})$$

where $\langle \hat{\sigma}_j \rangle_\eta = \text{Tr}\{\hat{\sigma}_j \hat{\eta}\}$ and $\langle \hat{\sigma}_j \rangle_\rho = \text{Tr}\{\hat{\sigma}_j \hat{\rho}_p^{(s)}\}$. Since $\langle \hat{\sigma}_x \rangle_\eta = \eta_{LH} + \eta_{HL}$, $\langle \hat{\sigma}_y \rangle_\eta = i(\eta_{HL} - \eta_{LH})$, $\langle \hat{\sigma}_z \rangle_\eta = \eta_{HH} -$

η_{LL} , $\langle \hat{\sigma}_x \rangle_\rho = c_x$, $\langle \hat{\sigma}_y \rangle_\rho = c_y$, and $\langle \hat{\sigma}_z \rangle_\rho = c_z$, Eq. (C2) is rewritten as $L(c_x, c_y, c_z) = (c_x - \bar{c}_x)^2 + (c_y - \bar{c}_y)^2 + (c_z - \bar{c}_z)^2 + \dots$, where

$$\bar{c}_x = \text{Re}(\eta_{LH} + \eta_{HL}), \quad (\text{C3})$$

$$\bar{c}_y = \text{Im}(\eta_{LH} - \eta_{HL}), \quad (\text{C4})$$

$$\bar{c}_z = \text{Re}(\eta_{HH} - \eta_{LL}). \quad (\text{C5})$$

Therefore, if point $R(\bar{c}_x, \bar{c}_y, \bar{c}_z)$ is inside of the unit sphere, L is minimized at this point. On the other hand, if point R is out of the unit sphere, L is minimized at the projection of point R to the unit sphere. Therefore,

$$(c_x, c_y, c_z) = \frac{(\bar{c}_x, \bar{c}_y, \bar{c}_z)}{\max(1, \sqrt{\bar{c}_x^2 + \bar{c}_y^2 + \bar{c}_z^2})}. \quad (\text{C6})$$

In Table II, we present the measured matrix elements of $\hat{\eta}$ and the estimated Bloch vector components (c_x, c_y, c_z) for various input photon numbers $|\alpha|^2$. The initial atom-qubit state is chosen as $|\psi_a\rangle = (|g\rangle - i|e\rangle)/\sqrt{2}$ for example. The state-transfer fidelity is that between the initial atom and final photon qubits, $F = \langle \psi_a | \hat{\rho}_p^{(s)} | \psi_a \rangle = (1 + c_y)/2$. We observe that the estimated density matrix is mostly insensitive to the input photon number $|\alpha|^2$. In Fig. 4(c), we employ the averaged density matrix over the four cases as $\hat{\rho}_p^{(s)}$.

APPENDIX D: EXPERIMENTAL INFORMATION

1. Experimental setup

Figure 7 shows a schematic of the measurement setup composed of room-temperature microwave instruments and low-temperature wirings with microwave components in a cryogen-free $^3\text{He}/^4\text{He}$ dilution refrigerator.

The photon-qubit (drive) pulses applied to port 1 (2) are generated by mixing the continuous microwave from rf source 1 (2) with pulses that have an IF generated by a digital-to-analog converter (DAC) with a sampling rate of 1 GHz. The Gaussian pulses are used for the photon-qubit pulses, while the flat-top pulses, in which the rising

TABLE II. Estimation of the final photon-qubit state in the atom-to-photon transfer experiment. The initial atom-qubit state is $|\psi_a\rangle = (|g\rangle - i|e\rangle)/\sqrt{2}$.

$ \alpha ^2$	η_{LL}	η_{LH}	η_{HL}	η_{HH}	c_x	c_y	c_z	Fidelity
0.048	0.515 + 0.057i	-0.095 + 0.187i	-0.003 - 0.277i	0.485 - 0.057i	-0.097	0.465	-0.030	0.732
0.101	0.509 + 0.043i	-0.113 + 0.215i	0.042 - 0.333i	0.491 - 0.043i	-0.071	0.548	-0.018	0.774
0.163	0.502 + 0.056i	-0.106 + 0.204i	0.030 - 0.282i	0.498 - 0.056i	-0.076	0.485	-0.004	0.743
0.206	0.503 + 0.058i	-0.121 + 0.162i	0.038 - 0.330i	0.497 - 0.058i	-0.083	0.492	-0.007	0.746
Average					-0.082	0.498	-0.015	0.749 ± 0.015

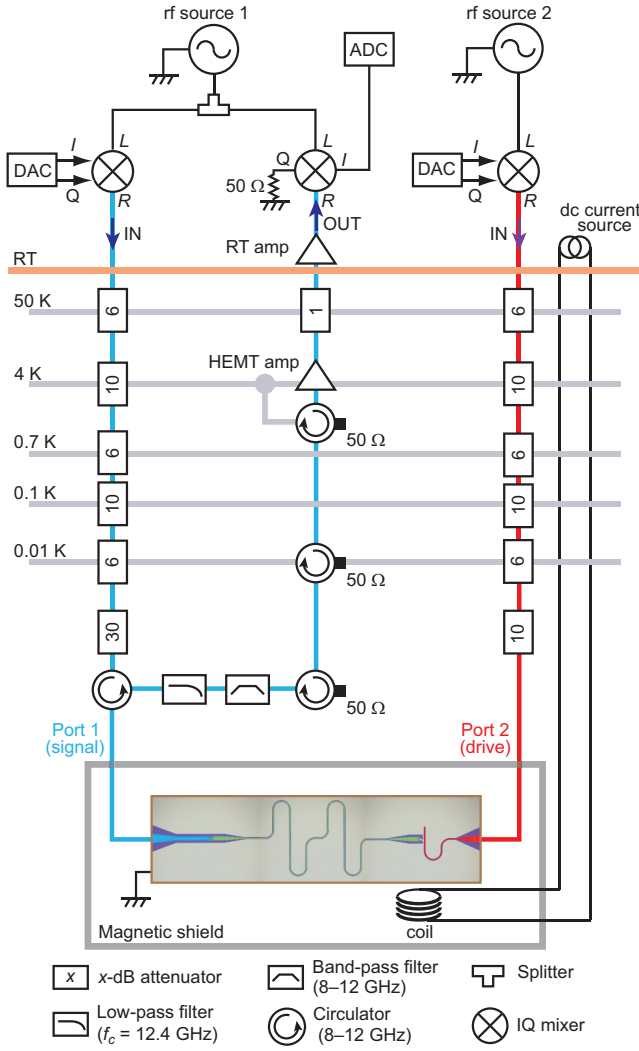


FIG. 7. Schematic of the experimental setup.

and falling edges of the pulse envelope are smoothed by a Gaussian function with full width at half maximum of 40 ns in its voltage amplitude, are employed for the drive pulses.

The signal pulses are heavily attenuated by a series of attenuators implemented in the input microwave semi-rigid cable with a total attenuation of 68 dB and applied to the $\lambda/2$ resonator through a circulator to separate the input and reflected signal. The reflected signal is led to a cryogenic HEMT amplifier mounted at a 4-K stage of the dilution refrigerator via low-pass and band-pass filters and three circulators with 50- Ω terminations and amplified by about 38 dB followed by further amplification with a room-temperature (RT) low-noise amplifier, whose gain is about 33 dB. The output signal is down-converted to an IF at an IQ mixer using the same continuous microwave split signal as used for the photon-qubit pulse generation. The I component of the reflected signals is sampled at 1.6 GHz/Sa by an analog-to-digital converter (ADC).

TABLE III. Device parameters for the photon-to-atom and atom-to-photon state-transfer experiments.

Parameters	Photon \rightarrow atom (GHz)	Atom \rightarrow photon (GHz)
$\omega_r/2\pi$	10.258	10.258
$\omega_{ge}/2\pi$	5.839	5.835
$2\chi/2\pi$	0.073	0.073
$\kappa/2\pi$	0.024	0.024
$\omega_d/2\pi$	5.785	5.775
$\omega_L/2\pi$	10.208	10.201
$\omega_H/2\pi$	10.266	10.263

The drive pulses are applied through the input microwave semi-rigid cable with a total attenuation of 48 dB to control the states of an atom.

2. Device and parameters

A device employed in our experiments is composed of a $\lambda/2$ superconducting coplanar waveguide resonator and a superconducting flux qubit containing three Josephson junctions [Fig. 1(b)]. They are coupled capacitively and operated in the dispersive regime. The flux qubit is always biased with a half flux quantum and we demonstrate all the experiments presented in the article. We adopted the same design and fabrication processes for the device described in Refs. [17,36].

In Table III, we summarize the system parameters for the photon-to-atom and atom-to-photon state-transfer experiments described in the main text. Since each experiment was performed in the different cooling down of our dilution refrigerator, ω_{ge} and related parameters (χ , ω_d , ω_L , and ω_H) changed slightly. The other parameters (ω_r and κ) are independent of ω_{ge} and remain unchanged.

3. Readout fidelity

The readout fidelity of a flux qubit used in our experiment was measured by applying a pulse sequence shown in the tomography regime of Fig. 3(a). In Fig. 8, we show normalized amplitudes of the reflection coefficient $|\Gamma'|$ of the readout resonator when the flux qubit is in the $|g\rangle$ and the $|e\rangle$ states. For the latter, we apply a π pulse [corresponding to the control pulse in Fig. 3(a)] with a width of 6 ns before a readout pulse. We normalize Γ' as $\Gamma' \equiv (\Gamma - \Gamma_{\text{on}})/|\Gamma_{\text{off}} - \Gamma_{\text{on}}|$, where Γ is the reflection coefficient measured in the experiment and Γ_{on} and Γ_{off} are obtained on and off resonances of the resonator, respectively. The off resonance Γ_{off} , which is the averaged value of Γ for the $|g\rangle$ state of the qubit from 10.0 to 10.2 GHz (201 points), is used as a reference. When the flux qubit is in the $|g\rangle$ state, a dip corresponding to the resonance is observed at $\omega_r/2\pi = 10.258$ GHz, where $|\Gamma'| = 0$, while the dip is shifted to $(\omega_r - 2\chi)/2\pi = 10.185$ GHz when

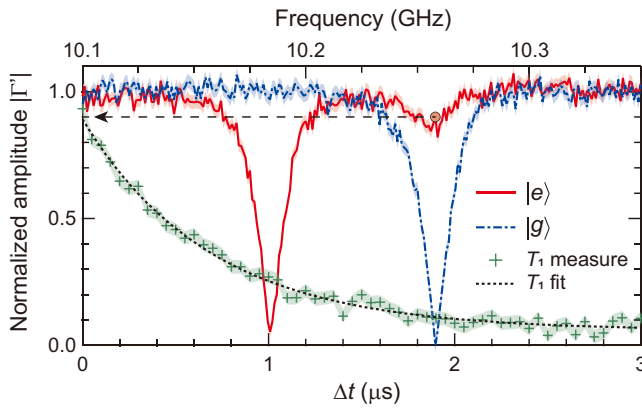


FIG. 8. Normalized readout amplitude as functions of the probe frequency (upper axis) and delay time Δt (bottom axis) between the π and the readout pulses. The dash-dot (blue) and solid (red) curves were measured when the qubit was in the $|g\rangle$ and the $|e\rangle$ states, respectively. The measured cross points (green) show the typical T_1 decay, whose fit to the exponential function (black dotted curve) gives a T_1 of about 700 ns. The circle indicates the readout amplitude at $\omega_r/2\pi = 10.258$ GHz, which corresponds to the readout fidelity of the flux qubit and the initial $|\Gamma'\rangle$ of the exponential decay (indicated by the dashed arrow). Shaded areas on the measured curves represent error bars of the normalized amplitudes caused by the averaged Γ_{off} .

we apply a π pulse to the flux qubit. Here 2χ is the dispersive frequency shift. We observed $2|\chi|/2\pi = 0.073$ GHz in the experiment, which was enhanced by an effect of the straddling regime [42]. The residual dip at $\omega_r/2\pi$ for the flux qubit in the $|e\rangle$ state is caused by the energy relaxation of the qubit before readout, and its amplitude gives the readout fidelity of the flux qubit (indicating the circle in Fig. 8). The duration of the readout pulse shown in Fig. 3(a) is 400 ns. However, we acquire a first 100-ns time trace at 1.6 GHz/Sa to extract the amplitude and the phase after waiting for about 70 ns, which is mainly required for the transient response of the electromagnetic field in the resonator [42]. The exponential decay of $|\Gamma'|$ in Fig. 8 is measured by changing the delay time Δt between the π and the readout pulses. The initial value of $|\Gamma'|$, corresponding to the circle in Fig. 8 (also indicated by the dashed arrow), is about 0.90 [= $\exp(-70/T_1)$], where $T_1 \sim 700$ ns. The T_1 of the flux qubit fluctuates with a relatively long period (about a few hours). Typically, T_1 is approximately 900 ns, but as the data set in Fig. 8 shows, there are times when T_1 is about 700 ns. In the state-transfer experiments shown in Figs. 3 and 4, T_1 is monitored before and after the measurement to confirm that T_1 is about 900 ns.

- [2] Y. Wu, *et al.*, Strong quantum computational advantage using a superconducting quantum processor, *Phys. Rev. Lett.* **127**, 180501 (2021).
- [3] J. I. Cirac, A. K. Ekert, S. F. Huelga, and C. Macchiavello, Distributed quantum computation over noisy channels, *Phys. Rev. A* **59**, 4249 (1999).
- [4] Y. L. Lim, A. Beige, and L. C. Kwek, Repeat-until-success linear optics distributed quantum computing, *Phys. Rev. Lett.* **95**, 030505 (2005).
- [5] D. Cuomo, M. Caleffi, and A. S. Cacciapuoti, Towards a distributed quantum computing ecosystem, *IET Quantum Commun.* **1**, 3 (2020).
- [6] S. Bravyi, O. Dial, J. M. Gambetta, D. Gil, and Z. Nazario, The future of quantum computing with superconducting qubits, *J. Appl. Phys.* **132**, 160902 (2022).
- [7] A. Reiserer and G. Rempe, Cavity-based quantum networks with single atoms and optical photons, *Rev. Mod. Phys.* **87**, 1379 (2015).
- [8] N. Meher and S. Sivakumar, A review on quantum information processing in cavities, *Eur. Phys. J. Plus* **137**, 985 (2022).
- [9] J. T. Shen and S. Fan, Coherent photon transport from spontaneous emission in one-dimensional waveguides, *Opt. Lett.* **30**, 2001 (2005).
- [10] O. Astafiev, A. M. Zagoskin, A. A. Abdumalikov Jr, Y. A. Pashkin, T. Yamamoto, K. Inomata, Y. Nakamura, and J. S. Tsai, Resonance fluorescence of a single artificial atom, *Science* **327**, 840 (2010).
- [11] I. C. Hoi, C. M. Wilson, G. Johansson, J. Lindkvist, B. Peropadre, T. Palomaki, and P. Delsing, Microwave quantum optics with an artificial atom in one-dimensional open space, *New J. Phys.* **15**, 025011 (2013).
- [12] A. F. van Loo, A. Fedorov, K. Lalumiere, B. C. Sanders, A. Blais, and A. Wallraff, Photon-mediated interactions between distant artificial atoms, *Science* **342**, 1494 (2013).
- [13] X. Gu, A. F. Kockum, A. Miranowicz, Y. X. Liu, and F. Nori, Microwave photonics with superconducting quantum circuits, *Phys. Rep.* **718-719**, 1 (2017).
- [14] S. Kono, K. Koshino, D. Lachance-Quirion, A. F. van Loo, Y. Tabuchi, A. Noguchi, and Y. Nakamura, Breaking the trade-off between fast control and long lifetime of a superconducting qubit, *Nat. Commun.* **11**, 3683 (2020).
- [15] A. Blais, A. L. Grimsmo, S. M. Girvin, and A. Wallraff, Circuit quantum electrodynamics, *Rev. Mod. Phys.* **93**, 25005 (2021).
- [16] K. Koshino, K. Inomata, Z. Lin, Y. Nakamura, and T. Yamamoto, Theory of microwave single-photon detection using an impedance-matched Λ system, *Phys. Rev. A* **91**, 043805 (2015).
- [17] K. Inomata, Z. R. Lin, K. Koshino, W. D. Oliver, J. S. Tsai, T. Yamamoto, and Y. Nakamura, Single microwave-photon detector using an artificial Λ -type three-level system, *Nat. Commun.* **7**, 12303 (2016).
- [18] J. Govenius, R. E. Lake, K. Y. Tan, and M. Mottonen, Detection of zeptojoule microwave pulses using electrothermal feedback in proximity-induced Josephson junctions, *Phys. Rev. Lett.* **117**, 030802 (2016).
- [19] S. Kono, K. Koshino, Y. Tabuchi, A. Noguchi, and Y. Nakamura, Quantum non-demolition detection of an itinerant microwave photon, *Nat. Phys.* **14**, 546 (2018).

[1] F. Arute, *et al.*, Quantum supremacy using a programmable superconducting processor, *Nature* **574**, 505 (2019).

- [20] J.-C. Besse, S. Gasparinetti, M. C. Collodo, T. Walter, P. Kurpiers, M. Pechal, C. Eichler, and A. Wallraff, Single-shot quantum nondemolition detection of individual itinerant microwave photons, *Phys. Rev. X* **8**, 021003 (2018).
- [21] R. Lescanne, S. Deleglise, E. Albertinale, U. Reglade, T. Capelle, E. Ivanov, T. Jacqmin, Z. Leghtas, and E. Flurin, Irreversible qubit-photon coupling for the detection of itinerant microwave photons, *Phys. Rev. X* **10**, 021038 (2020).
- [22] J. I. Cirac, P. Zoller, H. J. Kimble, and H. Mabuchi, Quantum state transfer and entanglement distribution among distant nodes in a quantum network, *Phys. Rev. Lett.* **78**, 3221 (1997).
- [23] Y. Yin, Y. Chen, D. Sank, P. J. J. O'Malley, T. C. White, R. Barends, J. Kelly, E. Lucero, M. Mariantoni, A. Megrant, C. Neill, A. Vainsencher, J. Wenner, A. N. Korotkov, A. N. Cleland, and J. M. Martinis, Catch and release of microwave photon states, *Phys. Rev. Lett.* **110**, 107001 (2013).
- [24] M. Pechal, L. Huthmacher, C. Eichler, S. Zeytinoglu, A. A. Abdumalikov, Jr. S. Berger, A. Wallraff, and S. Filip, Microwave-controlled generation of shaped single photons in circuit quantum electrodynamics, *Phys. Rev. X* **4**, 041010 (2014).
- [25] P. Kurpiers, P. Magnard, T. Walter, B. Royer, M. Pechal, J. Heinsoo, Y. Salathe, A. Akin, S. Storz, J.-C. Besse, S. Gasparinetti, A. Blais, and A. Wallraff, Deterministic quantum state transfer and remote entanglement using microwave photons, *Nature* **558**, 264 (2018).
- [26] P. Campagne-Ibarcq, E. Zaly-Geller, A. Narla, S. Shankar, P. Reinhold, L. Burkhardt, C. Axline, W. Pfaff, L. Frunzio, R. J. Schoelkopf, and M. H. Devoret, Deterministic remote entanglement of superconducting circuits through microwave two-photon transitions, *Phys. Rev. Lett.* **120**, 200501 (2018).
- [27] N. Leung, Y. Lu, S. Chakram, R. K. Naik, N. Earnest, R. Ma, K. Jacobs, A. N. Cleland, and D. I. Schuster, Deterministic bidirectional communication and remote entanglement generation between superconducting qubits, *npj Quantum inf.* **5**, 18 (2019).
- [28] K. Reuer, J. C. Besse, L. Wernli, P. Magnard, P. Kurpiers, G. J. Norris, A. Wallraff, and C. Eichler, Realization of a universal quantum gate set for itinerant microwave photons, *Phys. Rev. X* **12**, 011008 (2022).
- [29] Y. P. Zhong, H.-S. Chang, K. J. Satzinger, M.-H. Chou, A. Bienfait, C. R. Conner, E. Dumur, J. Grebel, G. A. Peairs, R. G. Povey, D. I. Schuster, and A. N. Cleland, Violating Bell's inequality with remotely connected superconducting qubits, *Nat. Phys.* **15**, 741 (2019).
- [30] Jiawei Qiu, Yang Liu, Jingjing Niu, Ling Hu, Yukai Wu, Libo Zhang, Wenhui Huang, Yuanzhen Chen, Jian Li, Song Liu, Youpeng Zhong, Luming Duan, and Dapeng Yu, Deterministic quantum teleportation between distant superconducting chips, [arXiv:2302.08756](https://arxiv.org/abs/2302.08756).
- [31] K. Koshino, K. Inomata, Z. R. Lin, Y. Tokunaga, T. Yamamoto, and Y. Nakamura, Theory of deterministic entanglement generation between remote superconducting atoms, *Phys. Rev. Appl.* **7**, 064006 (2017).
- [32] D. Pinotsi and A. Imamoglu, Single photon absorption by a single quantum emitter, *Phys. Rev. Lett.* **100**, 093603 (2008).
- [33] K. Koshino, S. Ishizaka, and Y. Nakamura, Deterministic photon-photon (SWAP)^{1/2} gate using a Λ system, *Phys. Rev. A* **82**, 010301(R) (2010).
- [34] D. Witthaut and A. S. Sorensen, Photon scattering by a three-level emitter in a one-dimensional waveguide, *New J. Phys.* **12**, 043052 (2010).
- [35] K. Koshino, K. Inomata, T. Yamamoto, and Y. Nakamura, Implementation of an impedance-matched Λ system by dressed-state engineering, *Phys. Rev. Lett.* **111**, 153601 (2013).
- [36] K. Inomata, K. Koshino, Z. R. Lin, W. D. Oliver, J. S. Tsai, Y. Nakamura, and T. Yamamoto, Microwave down-conversion with an impedance-matched Λ system in driven circuit QED, *Phys. Rev. Lett.* **113**, 063064 (2014).
- [37] I. Shomroni, S. Rosenblum, Y. Lovsky, O. Bechler, G. Guendelman, and B. Dayan, All-optical routing of single photons by a one-atom switch controlled by a single photon, *Science* **345**, 903 (2014).
- [38] S. Rosenblum, O. Bechler, I. Shomroni, Y. Lovsky, G. Guendelman, and B. Dayan, Extraction of a single photon from an optical pulse, *Nat. Photonics* **10**, 19 (2016).
- [39] O. Bechler, A. Borne, S. Rosenblum, G. Guendelman, O. E. Mor, M. Netser, T. Ohana, Z. Aqua, N. Drucker, R. Finkelstein, Y. Lovsky, R. Bruch, D. Gurovich, E. Shafir, and B. Dayan, A passive photon-atom qubit swap operation, *Nat. Phys.* **14**, 996 (2018).
- [40] A. Blais, R.-S. Huang, A. Wallraff, S. M. Girvin, and R. J. Schoelkopf, Cavity quantum electrodynamics for superconducting electrical circuits: An architecture for quantum computation, *Phys. Rev. A* **69**, 062320 (2004).
- [41] P. Krantz, M. Kjaergaard, F. Yan, T. P. Orlando, S. Gustavsson, and W. D. Oliver, A quantum engineer's guide to superconducting qubits, *Appl. Phys. Rev.* **6**, 021318 (2019).
- [42] K. Inomata, T. Yamamoto, P.-M. Billangeon, Y. Nakamura, and J. S. Tsai, Large dispersive shift of cavity resonance induced by a superconducting flux qubit in the straddling regime, *Phys. Rev. B* **86**, 140508 (2012).
- [43] G. Burkard, D. Loss, and D. P. DiVincenzo, Coupled quantum dots as quantum gates, *Phys. Rev. B* **59**, 2070 (1999).
- [44] H. Fan, V. Roychowdhury, and T. Szkopek, Optimal two-qubit quantum circuits using exchange interactions, *Phys. Rev. A* **72**, 052323 (2005).
- [45] Y. Zhou and G.-F. Zhang, (swap) ^{α} gate in the presence of spin-orbit coupling in coupled quantum dots, *Opt. Commun.* **316**, 22 (2014).
- [46] W. Q. Liu and H. R. Wei, Implementations of more general solid-state (SWAP)^{1/m} and controlled-(swap)^{1/m} gates, *New J. Phys.* **21**, 103018 (2019).
- [47] S. Clemmen, A. Farsi, S. Ramelow, and A. L. Gaeta, Ramsey interference with single photons, *Phys. Rev. Lett.* **117**, 223601 (2016).
- [48] J. M. Lukens and P. Lougovski, Frequency-encoded photonic qubits for scalable quantum information processing, *Optica* **4**, 8 (2017).
- [49] S. C. Connell, J. Scarabel, E. M. Bridge, K. Shimizu, V. Blums, M. Ghadimi, M. Lobino, and E. W. Streed,

- Ion-photonic frequency qubit correlations for quantum networks, *J. Phys. B: At. Mol. Opt. Phys.* **54**, 175503 (2021).
- [50] M. L. Chan, Z. Aqua, A. Tiranov, B. Dayan, P. Lodahl, and A. S. Sorensen, Quantum state transfer between a frequency-encoded photonic qubit and a quantum-dot spin in a nanophotonic waveguide, *Phys. Rev. A* **105**, 062445 (2022).
- [51] J. Ilves, S. Kono, Y. Sunada, S. Yamazaki, M. Kim, K. Koshino, and Y. Nakamura, On-demand generation and characterization of a microwave time-bin qubit, *npj Quantum Inf.* **6**, 34 (2020).